

# A micropolar shell formulation for hard-magnetic soft materials

Farzam Dadgar-Rad<sup>a</sup>, Mokarram Hossain<sup>b,\*</sup>

<sup>a</sup>*Faculty of Mechanical Engineering, University of Guilan, Rasht, Iran*

<sup>b</sup>*Zienkiewicz Centre for Computational Engineering, College of Engineering, Swansea University, SA1 8EN, UK*

---

## Abstract

Hard-magnetic soft materials (HMSMs) are particulate composites that consist of a soft matrix embedded with particles of high remnant magnetic induction. Since the application of an external magnetic flux induces a body couple in HMSMs, the Cauchy stress tensor in these materials is asymmetric, in general. Therefore, the micropolar continuum theory can be employed to capture the deformation of these materials. On the other hand, the geometries and structures made of HMSMs often possess small thickness compared to the overall dimensions of the body. Accordingly, in the present contribution, a 10-parameter micropolar shell formulation to model the finite elastic deformation of thin structures made of HMSMs and subject to magnetic stimuli is developed. The present shell formulation allows for using three-dimensional constitutive laws without any need for modification to apply the plane stress assumption in thin structures. Due to the highly nonlinear nature of the governing equations, a nonlinear finite element formulation for numerical simulations is also developed. To circumvent locking at large distortions, an enhanced assumed strain formulation is adopted. The performance of the developed formulation is examined in several numerical examples. It is shown that the proposed formulation is an effective tool for simulating the deformation of thin bodies made of HMSMs.

*Keywords:* Micropolar continuum, 10-parameter shell model, Hard-magnetic soft materials, Magneto-elasticity, Finite element method

---

---

\*Corresponding author.

*Email addresses:* dadgar@guilan.ac.ir (Farzam Dadgar-Rad), mokarram.hossain@swansea.ac.uk (Mokarram Hossain)

## 1. Introduction

Magneto-active soft materials consist of magnetizable particles embedded into a soft elastomeric matrix and exhibit large mechanical deformations under magnetic stimuli. These materials have found potential applications in, e.g., sensors, actuators, vibration absorbers, isolators, soft and flexible electronics, and soft robots (see, e.g., [1–6] and references therein). For the optimum and effective design of various devices made of these materials, it is essential to develop reliable theoretical formulations for predicting their response under various geometries and loading conditions.

Based on the type of the embedded particles, magneto-active soft materials are divided into two sub-classes, namely *soft-magnetic soft materials* (SMSMs) and *hard-magnetic soft materials* (HMSMs). The former contains particles with low coercivity, such as iron or iron oxides, and their magnetization vector changes by applying external magnetic stimuli. This sub-class has been the subject of a huge amount of research work in the past two decades (e.g., [7–13]). The latter sub-class is composed of particles, such as  $\text{CoFe}_2\text{O}_4$  or  $\text{NdFeB}$ , that have a high coercivity, and their magnetization vector, or equivalently, their remnant magnetic flux, remains unchanged for a wide range of the applied external magnetic flux (e.g., [14, 15]). One of the main characteristics of HMSMs is that they quickly undergo large deformations under relatively small values of external magnetic induction (e.g., [16, 17]). Moreover, using the 3D printing technologies, it is possible to program the local orientation of the magnetized particles, which leads to the desired complex deformations [18–22].

Theoretical modeling of HMSMs has been the subject of a plethora of research articles in recent years (e.g., [23–32]). In particular, Zhao et al. [24] developed a continuum formulation with an asymmetric Cauchy stress tensor, which is very similar to the classical continuum theory in the sense that it neither needs non-classical material parameters nor additional degrees of freedom. Their theory has been the foundation for the analysis of hard-magnetic soft beams (HMSBs) in Wang et al. [33], Chen et al. [34, 35], Rajan and Arockiarajan [36], and Yan et al. [37] among others. The same formulation has been employed to model the deformation of magneto-active shells by Yan et al. [38]. Dadgar-Rad and Hossain [39] added the viscoelastic effects to the theory of Zhao et al. [24] to analyze the time-dependent dissipative response of HMSBs. Micromechanical and lattice models for the deformation analysis of HMSMs have been also

formulated by Zhang et al. [28], Garcia-Gonzalez and Hossain [29, 30], and Ye et al. [31]. From a different point of view, Dadgar-Rad and Hossain [32] focused on the well-known phenomenon that the interaction between remnant and external magnetic fluxes induces a body couple on the continuum body (e.g., [40]). Therefore, the Cauchy stress in HMSMs is asymmetric, as had been previously pointed out by Zhao et al. [24]. However, instead of following the methodology advocated in [24], the authors developed a formulation based on micropolar continuum theory to model the finite deformation of three-dimensional bodies made of HMSMs. Two significant differences between the results of the formulation of Zhao et al. [24] and those based on the micropolar-enhanced formulation have been expressed by Dadgar-Rad and Hossain [32].

Eringen and his coworkers established the theoretical foundations of micropolar theory (e.g., [41–43]). In this theory, each material particle is associated with a micro-structure that can undergo rigid rotations independently from its surrounding medium. Formulations of the micropolar theory to model localized elastic-plastic deformations (e.g., [44–50]) and size-dependent elastic deformations (e.g., [51–56]) have been developed. Some formulations to model micropolar shells have been also proposed (e.g., [57–59]). Moreover, the theory has been used in the modeling of lattice structures, crystal plasticity, phononic crystals, chiral auxetic lattices, phase-field fracture mechanics, and vertebral trabecular bone (e.g., [60–65]).

The current research is essentially the continuation of the previous work of the authors, namely Dadgar-Rad and Hossain [32], which had been developed for three-dimensional bodies. However, most bodies made of HMSMs are thin structures, and using three-dimensional elements is computationally expensive. Therefore, the main objective of this work is to develop a shell formulation based on the micropolar continuum theory to predict the deformation of thin HMSMs. To do so, the 7-parameter shell formulation of Sansour (e.g., [66, 67]) has been extended to a 10-parameter one that takes into account the micro-rotation of the micropolar theory. On the other hand, one of the successful methods for eliminating locking effects in shell structures is the enhanced assumed strain method (EAS), e.g., [68–71]. Accordingly, this method is adopted here to circumvent locking effects in the present micropolar shell formulation.

The rest of this paper is organized as follows: In Section 2, the basic kinematic and kinetic relations of the micropolar continuum theory are presented. In Section 3, the main characteristics of hard-magnetic soft materials are introduced. The kinematic equations describing a

10-parameter micropolar shell model are provided in Section 4. The variational formulation of the problem is then formulated in Section 5. A nonlinear finite element formulation for the numerical simulation of the related problems is developed in Section 6. Several numerical examples are solved in Section 7. Finally, a summary of the work is provided in Section 8.

**Notation:** Throughout this work, all lower-case and upper-case Latin indices range over  $\{1, 2, 3\}$ , and Greek indices range over  $\{1, 2\}$ . Upper-case Latin indices with calligraphic font, e.g.,  $\mathcal{I}$  and  $\mathcal{J}$ , do not obey a general rule and take the specified values defined in the corresponding equations. The summation convention holds over all repeated Greek and Latin indices. For the two second-order tensors  $\mathbf{P}$  and  $\mathbf{Q}$ , the tensorial products defined based on the symbols  $\otimes$ ,  $\odot$ , and  $\boxtimes$  generate fourth-order tensors, so that the corresponding components are given by  $(\mathcal{C})_{ijkl} = (\mathbf{P} \otimes \mathbf{Q})_{ijkl} = P_{ij}Q_{kl}$ ,  $(\mathcal{B})_{ijkl} = (\mathbf{P} \odot \mathbf{Q})_{ijkl} = P_{ik}Q_{jl}$ , and  $(\mathcal{C})_{ijkl} = (\mathbf{P} \boxtimes \mathbf{Q})_{ijkl} = P_{il}Q_{kj}$ , respectively. The notations  $\text{tr} \mathbf{P}$ ,  $\mathbf{P}^\top$ ,  $\det \mathbf{P}$ ,  $\mathbf{P}^{-1}$ , and  $\mathbf{P}^{-\top}$  are the trace, transpose, determinant, inverse, and inverse transpose of the second-order tensor  $\mathbf{P}$ . For numerical simulations, the notation  $\mathbb{P} = \{P_{11}, P_{22}, P_{33}, P_{12}, P_{21}, P_{13}, P_{31}, P_{23}, P_{32}\}^\top$  will be used as the  $9 \times 1$  vectorial representation of the arbitrary second-order tensor  $\mathbf{P}$ .

## 2. A brief review of the micropolar continuum theory

Some fundamental relations of the micropolar continuum theory are presented in this section. The interested reader is referred to the pioneering works developed in Refs. [42, 43, 46] for more details and discussions.

In this section, to describe, respectively, the material and spatial quantities, two coincident Cartesian coordinate systems  $\{X_1, X_2, X_3\}$  and  $\{x_1, x_2, x_3\}$  are considered. The corresponding orthonormal basis vectors are denoted by  $\{\mathbf{e}_1, \mathbf{e}_2, \mathbf{e}_3\}$  and  $\{\mathbb{E}_1, \mathbb{E}_2, \mathbb{E}_3\}$ , respectively. The *right gradient* and *right divergence* operators of the form  $\text{Grad}\{\bullet\} = \frac{\partial\{\bullet\}}{\partial X_I} \otimes \mathbb{E}_I$ ,  $\text{Div}\{\bullet\} = \frac{\partial\{\bullet\}}{\partial X_I} \cdot \mathbb{E}_I$ ,  $\text{grad}\{\bullet\} = \frac{\partial\{\bullet\}}{\partial x_i} \otimes \mathbf{e}_i$ , and  $\text{div}\{\bullet\} = \frac{\partial\{\bullet\}}{\partial x_i} \cdot \mathbf{e}_i$  are used in this work.

Let  $\mathcal{B}_0$  and  $\mathcal{B}$  be the reference and current configurations of the continuum body at the times  $t = 0$  and  $t > 0$ , respectively. At each material point in  $\mathcal{B}_0$  a macro-element is considered, the center of which is denoted by  $\mathbb{X}$ . After deformation by the macro-deformation  $\boldsymbol{\psi}$ , the center of the macro-element in  $\mathcal{B}$  is denoted by  $\mathbf{x}$ , so that  $\mathbf{x} = \boldsymbol{\psi}(\mathbb{X}, t)$ . As usual, the local deformation

of the macro-element is described by the deformation gradient tensor  $\mathbf{F}$ , given by

$$\mathbf{F} = \text{Grad } \boldsymbol{\psi} = \frac{\partial x_i}{\partial X_I} \mathbf{e}_i \otimes \mathbb{E}_I, \quad J = \det \mathbf{F} > 0. \quad (1)$$

From the polar decomposition theorem, the deformation gradient is uniquely decomposed as  $\mathbf{F} = \mathbf{R}\mathbf{U} = \mathbf{V}\mathbf{R}$ . Here,  $\mathbf{R}$  is the macro-rotation tensor, and  $\mathbf{U}$  and  $\mathbf{V}$  are the symmetric positive definite right and the left stretch tensors, respectively. For later use, the variation of the deformation gradient is written as follows:

$$\delta \mathbf{F} = \text{Grad } \delta \hat{\mathbf{u}} = \delta \mathbf{Y} \mathbf{F} \quad \text{with} \quad (\delta \mathbf{Y})_{ij} \stackrel{\text{def}}{=} (\text{grad } \delta \hat{\mathbf{u}})_{ij} = \frac{\partial \delta \hat{u}_i}{\partial x_j}. \quad (2)$$

Moreover,  $\hat{\mathbf{u}} = \mathbf{x} - \mathbb{X}$  is the actual displacement field, and  $\delta \hat{\mathbf{u}} = \delta \mathbf{x}$  is the virtual displacement.

In the micropolar theory, it is assumed that there exists a micro-structure inside each macro-element so that it experiences rigid micro-rotations independent of the macro-motion  $\mathbf{x}$ . Let  $\boldsymbol{\theta} = \theta_i \mathbf{e}_i$  denote the micro-rotation pseudo-vector, and  $\theta = (\theta_i \theta_i)^{1/2}$  be its magnitude. The micro-rotation tensor  $\tilde{\mathbf{R}}$  corresponding to  $\boldsymbol{\theta}$  can be expressed via the Euler–Rodriguez formula, namely (e.g., [46, 52])

$$\tilde{\mathbf{R}}(\boldsymbol{\theta}) = \exp \hat{\boldsymbol{\theta}} = \mathbf{I} + \frac{\sin \theta}{\theta} \hat{\boldsymbol{\theta}} + \frac{1 - \cos \theta}{\theta^2} \hat{\boldsymbol{\theta}}^2, \quad (3)$$

where  $\hat{\boldsymbol{\theta}} = -\boldsymbol{\mathcal{E}}\boldsymbol{\theta}$ , or  $\hat{\theta}_{ij} = -\epsilon_{ijk}\theta_k$ , is the skew-symmetric tensor corresponding to  $\boldsymbol{\theta}$ . Moreover,  $\epsilon_{ijk}$  are the components of the alternating symbol  $\boldsymbol{\mathcal{E}}$ . By defining  $\delta \boldsymbol{\theta}$  as the virtual micro-rotation pseudo-vector, the variation of  $\tilde{\mathbf{R}}$  may be expressed via the following relations [32, 52]

$$\left. \begin{aligned} \delta \tilde{\mathbf{R}} &= \delta \hat{\boldsymbol{\omega}} \tilde{\mathbf{R}} \quad \text{with} \quad \delta \hat{\boldsymbol{\omega}} = -\boldsymbol{\mathcal{E}} \delta \boldsymbol{\omega}, \quad \delta \boldsymbol{\omega} = \boldsymbol{\Lambda} \delta \boldsymbol{\theta} \\ \text{and} \quad \boldsymbol{\Lambda} &= \frac{\sin \theta}{\theta} \mathbf{I} + \frac{1 - \cos \theta}{\theta^2} \hat{\boldsymbol{\theta}} + \frac{\theta - \sin \theta}{\theta^3} \boldsymbol{\theta} \otimes \boldsymbol{\theta} \end{aligned} \right\}. \quad (4)$$

The deformation gradient, in the micropolar theory, is decomposed as  $\mathbf{F} = \tilde{\mathbf{R}}\tilde{\mathbf{U}} = \tilde{\mathbf{V}}\tilde{\mathbf{R}}$ , which is apparently similar to the classical polar decomposition. The deformation tensors  $\tilde{\mathbf{U}}$  and  $\tilde{\mathbf{V}}$  are then defined by (e.g., [46]):

$$\tilde{\mathbf{U}} = \tilde{\mathbf{R}}^\top \mathbf{F}, \quad \tilde{U}_{IJ} = \tilde{R}_{nI} F_{nJ}, \quad \tilde{\mathbf{V}} = \mathbf{F} \tilde{\mathbf{R}}, \quad \tilde{V}_{ij} = F_{iN} \tilde{R}_{jN}. \quad (5)$$

It is noted that in contrast to  $\mathbf{U}$  and  $\mathbf{V}$  in the classical theory, the micropolar deformation tensors  $\tilde{\mathbf{U}}$  and  $\tilde{\mathbf{V}}$  are not symmetric, in general.

To take the gradient of the micro-rotation into account, the material wryness tensor  $\mathbf{\Gamma}$  and the spacial one  $\boldsymbol{\gamma}$ , are defined by [42, 43, 46, 53]

$$\mathbf{\Gamma} = -\frac{1}{2}\boldsymbol{\mathcal{E}}:(\tilde{\mathbf{R}}^\top \text{Grad} \tilde{\mathbf{R}}), \quad \Gamma_{IJ} = -\frac{1}{2}\epsilon_{IKL}\tilde{R}_{iK}\tilde{R}_{iL,J}, \quad \boldsymbol{\gamma} = \tilde{\mathbf{R}}\mathbf{\Gamma}\tilde{\mathbf{R}}^\top, \quad \gamma_{ij} = \tilde{R}_{iI}\Gamma_{IJ}\tilde{R}_{jJ}. \quad (6)$$

The deformation measures  $\tilde{\mathbf{U}}$  and  $\mathbf{\Gamma}$  are the main kinematic tensors to develop a formulation in material framework (see also, Refs. [42, 46]). Combinations of Eqs. (2), (4), (5)<sub>1</sub>, and (6)<sub>1</sub>, leads to the following expressions for the virtual kinematic tensor  $\delta\tilde{\mathbf{U}}$  and  $\delta\mathbf{\Gamma}$  [32]:

$$\delta\tilde{\mathbf{U}} = \tilde{\mathbf{R}}^\top(\delta\mathbf{Y} - \delta\hat{\boldsymbol{\omega}})\mathbf{F}, \quad \delta\mathbf{\Gamma} = \tilde{\mathbf{R}}^\top \text{Grad} \delta\boldsymbol{\omega} = \tilde{\mathbf{R}}^\top \text{grad} \delta\boldsymbol{\omega}\mathbf{F}. \quad (7)$$

Next, let  $d\mathcal{A}$  and  $\mathbf{n}$  be an infinitesimal area element and its outward unit normal vector in the current configuration, respectively. In the micropolar theory, besides the classical traction vector  $\mathfrak{t}^{(\mathbf{n})}$ , the couple vector  $\mathfrak{s}^{(\mathbf{n})}$  also acts on  $d\mathcal{A}$ . Accordingly, there exist the asymmetric Cauchy stress  $\boldsymbol{\sigma}$  and the couple stress tensor  $\mathbf{m}$  so that

$$\mathfrak{t}^{(\mathbf{n})} = \boldsymbol{\sigma}\mathbf{n}, \quad t_i^{(\mathbf{n})} = \sigma_{ij}n_j, \quad \mathfrak{s}^{(\mathbf{n})} = \mathbf{m}\mathbf{n}, \quad s_i^{(\mathbf{n})} = m_{ij}n_j. \quad (8)$$

For later use, the *first Piola–Kirchhoff* type stress and couple stress  $\{\mathbf{P}, \mathbf{M}\}$ , and the *material* stress and couple stress  $\{\tilde{\mathbf{P}}, \tilde{\mathbf{M}}\}$  are defined by

$$\{\mathbf{P}, \mathbf{M}\} = J\{\boldsymbol{\sigma}, \mathbf{m}\}\mathbf{F}^{-\top}, \quad \{\tilde{\mathbf{P}}, \tilde{\mathbf{M}}\} = \tilde{\mathbf{R}}^\top\{\mathbf{P}, \mathbf{M}\} = J\tilde{\mathbf{R}}^\top\{\boldsymbol{\sigma}, \mathbf{m}\}\mathbf{F}^{-\top}. \quad (9)$$

Following the standard procedures, the *spatial* and *material* descriptions of the balance of linear and angular momentum will be as follows (e.g., Refs. [32, 42, 43, 46]):

$$\left. \begin{aligned} \text{div} \boldsymbol{\sigma} + \mathbf{f} &= \mathbf{0}, & \text{Div} \mathbf{P} + \mathbf{f}^* &= \mathbf{0} \\ \text{div} \mathbf{m} - \boldsymbol{\mathcal{E}}:\boldsymbol{\sigma} + \mathbf{p} &= \mathbf{0}, & \text{Div} \mathbf{M} - \boldsymbol{\mathcal{E}}:\mathbf{P} + \mathbf{p}^* &= \mathbf{0} \end{aligned} \right\}, \quad (10)$$

where inertia effects have been neglected. Moreover,  $(\mathbf{f}, \mathbf{f}^* = J\mathbf{f})$  and  $(\mathbf{p}, \mathbf{p}^* = J\mathbf{p})$  are the body force and body couple per unit current and reference volume, respectively.

### 3. Basic relations of hard-magnetic soft materials

The main property of HMSMs is the existence of a remnant magnetic flux density, that remains almost unchanged under a wide range of the applied external magnetic flux  $\mathbb{B}^{\text{ext}}$  (e.g.,

[16, 17, 24]). Let  $\tilde{\mathbb{B}}^{\text{rem}}$  and  $\mathbb{B}^{\text{rem}}$  be the remnant magnetic flux in the reference and current configurations, respectively. The relation between  $\tilde{\mathbb{B}}^{\text{rem}}$  and  $\mathbb{B}^{\text{rem}}$  is as follows [24]:

$$\mathbb{B}^{\text{rem}} = J^{-1} \mathbf{F} \tilde{\mathbb{B}}^{\text{rem}}, \quad B_i^{\text{rem}} = J^{-1} F_{iJ} \tilde{B}_J^{\text{rem}}. \quad (11)$$

The action of  $\mathbb{B}^{\text{ext}}$  on  $\mathbb{B}^{\text{rem}}$  leads to a body couple that acts on the material points. By using the same notations  $\mathbb{p}$  and  $\mathbb{p}^*$  as introduced in the previous section, the magnetic body couple per unit reference volume is given by (e.g., [24, 40])

$$\mathbb{p}^* = J\mathbb{p} = \frac{J}{\mu_0} \mathbb{B}^{\text{rem}} \times \mathbb{B}^{\text{ext}} = \frac{1}{\mu_0} (\mathbf{F} \tilde{\mathbb{B}}^{\text{rem}}) \times \mathbb{B}^{\text{ext}}, \quad (12)$$

where the constant  $\mu_0 = 4\pi \times 10^{-7} \frac{N}{A^2}$  is the free space magnetic permeability.

For HMSMs, it is often assumed that the external magnetic flux density is uniform in space (e.g., Refs. [24, 33–36]). Accordingly, Zhao et al. [24] showed that the Maxwell equations of the following form are satisfied in HMSMs (e.g., [40]):

$$\text{Curl} \mathbb{H} = \epsilon_{IJK} H_{J,K} \mathbb{E}_I = \mathbf{0}, \quad \text{Div} \mathbb{B} = B_{I,I} = 0, \quad (13)$$

where  $\mathbb{H}$  is the referential magnetic field,  $\mathbb{B}$  is the referential magnetic flux density, and "Curl" is the referential curl operator.

#### 4. Kinematics of a 10-parameter micropolar shell model

The geometry of a part of a shell in the reference configuration  $\mathcal{B}_0$  and the current configuration  $\mathcal{B}$  is displayed in Fig. 1. Mid-surface of the shell in the reference configurations is denoted by  $\mathcal{S}_0$ , which deforms into the surface  $\mathcal{S}$  in the current configuration. As shown in Fig. 1, in addition to the two common-frame Cartesian coordinates  $\{X_1 X_2 X_3\}$  and  $\{x_1 x_2 x_3\}$ , described in the previous section, the convective coordinate system  $\{\zeta^1 \zeta^2 \zeta^3\}$  at each material particle  $q$  of the reference mid-surface  $\mathcal{S}_0$  is also constructed. The coordinate lines  $\zeta^i$  deform during the motion of the shell in space so that the coordinated lines  $\zeta^1$  and  $\zeta^2$  are tangent to both  $\mathcal{S}_0$  and  $\mathcal{S}$ . Moreover, the coordinated line  $\zeta^3 \in [-\frac{1}{2}h, \frac{1}{2}h]$ , with  $h$  as the initial thickness of the shell, is considered to be perpendicular to  $\mathcal{S}_0$  in the reference configuration. However, it does not remain perpendicular to  $\mathcal{S}$  in the current configuration, in general. In the sequel, for the sake of simplicity, the coordinate  $\zeta^3$  may be replaced by  $z$ .

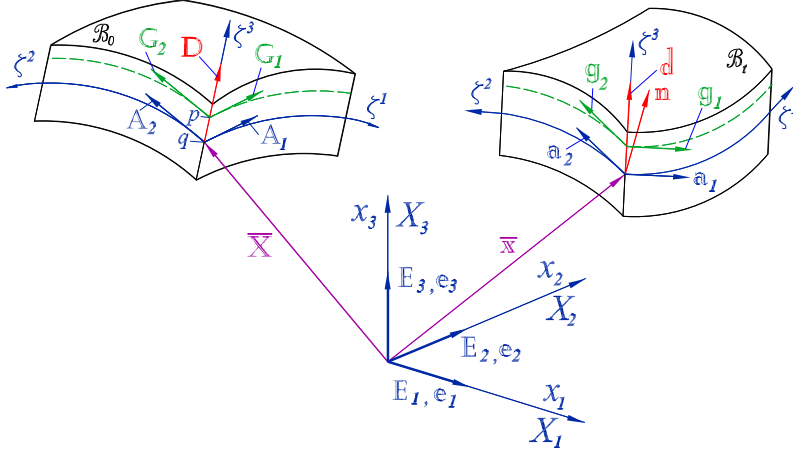


Figure 1: Schematic view of the deformation of a shell

The position of the material particle  $q$  on the mid-surface  $\mathcal{S}_0$  may be described by the vector  $\bar{\mathbb{X}}(\zeta^1, \zeta^2)$ . Let  $\{\mathbb{A}_\alpha, \mathbb{A}^\alpha, A_{\alpha\beta}, A^{\alpha\beta}, \mathbb{D}, \mathbb{B}\}$  be, respectively, the covariant and contravariant basis vectors, covariant and contravariant components of the metric tensor, outward unit normal vector, and the curvature tensor on the undeformed mid-surface  $\mathcal{S}_0$ . Then the following relations hold (e.g., [72]):

$$\left. \begin{aligned} \mathbb{A}_\alpha &= \frac{\partial \bar{\mathbb{X}}}{\partial \zeta^\alpha}, & A_{\alpha\beta} &= \mathbb{A}_\alpha \cdot \mathbb{A}_\beta, & A^{\alpha\eta} A_{\eta\beta} &= \delta_\beta^\alpha, & \mathbb{A}^\alpha &= A^{\alpha\beta} \mathbb{A}_\beta, & \mathbb{A}_\alpha \cdot \mathbb{A}^\beta &= \delta_\alpha^\beta \\ A &= \det[A_{\alpha\beta}], & \mathbb{D} &= \mathbb{A}_3 = \mathbb{A}^3 = \frac{\mathbb{A}_1 \times \mathbb{A}_2}{|\mathbb{A}_1 \times \mathbb{A}_2|} = \frac{\mathbb{A}_1 \times \mathbb{A}_2}{\sqrt{A}}, & \mathbb{B} &= -\mathbb{D}_{,\alpha} \otimes \mathbb{A}^\alpha \end{aligned} \right\}, \quad (14)$$

where  $\delta_\alpha^\beta$  is the two-dimensional Kronecker delta. For later use, the surface contravariant basis vectors may be written as  $\mathbb{A}^\alpha = A^{*\alpha J} \mathbb{E}_J$ , where  $A^{*\alpha J}$  are the Cartesian components of  $\mathbb{A}^\alpha$ . The position of the material particle  $p$  located at the elevation  $z$  with respect to  $\mathcal{S}_0$  is described by

$$\mathbb{X}(\zeta^1, \zeta^2, z) = \bar{\mathbb{X}}(\zeta^1, \zeta^2) + z\mathbb{D}(\zeta^1, \zeta^2), \quad (15)$$

from which the covariant basis vectors  $\mathbb{G}_i$  are obtained to be

$$\mathbb{G}_\alpha = \frac{\partial \mathbb{X}}{\partial \zeta^\alpha} = \mathbb{A}_\alpha + z\mathbb{D}_{,\alpha}, \quad \mathbb{G}_3 = \frac{\partial \mathbb{X}}{\partial z} = \mathbb{D}. \quad (16)$$

Motivated by Eqs. (14)<sub>8</sub> and (16), the symmetric shifter tensor  $\mathbf{Q} = \mathbf{Q}^\top = \mathbb{G}_i \otimes \mathbb{A}^i = \mathbf{I} - z\mathbf{B}$ , with  $\mathbf{I}$  as the identity tensor, is defined. Accordingly, it is possible to map the covariant and contravariant basis vectors from  $z \neq 0$  to the midsurface with  $z = 0$ , and vice versa. More precisely, the following relations hold:

$$\mathbb{G}_i = \mathbf{Q}\mathbb{A}_i, \quad \mathbb{A}_i = \mathbf{Q}^{-1}\mathbb{G}_i, \quad \mathbb{G}^i = \mathbf{Q}^{-1}\mathbb{A}^i, \quad \mathbb{A}^i = \mathbf{Q}\mathbb{G}^i, \quad (17)$$



where  $\mathbb{G}^i$  are the contravariant basis vectors at  $\mathbb{X}$ , and use has been made of the symmetry property of  $\mathbf{Q}$ . For later use, the three-dimensional material gradient operator  $\text{Grad}_\zeta$ , with respect to the convective coordinate system  $\{\zeta^1\zeta^2\zeta^3\}$  in the reference configuration, and the material surface gradient operator  $\text{Grad}_{\mathcal{S}_0}$  with respect to  $\{\zeta^1\zeta^2\}$  are defined as follows:

$$\text{Grad}_\zeta\{\bullet\} = \frac{\partial\{\bullet\}}{\partial\zeta^i} \otimes \mathbb{G}^i, \quad \text{Grad}_{\mathcal{S}_0}\{\bullet\} = \frac{\partial\{\bullet\}}{\partial\zeta^\alpha} \otimes \mathbb{A}^\alpha. \quad (18)$$

By assuming that a straight material fiber perpendicular to  $\mathcal{S}_0$  remains straight during deformation, the following macro deformation field is considered (e.g., [66, 67]):

$$\mathbf{x} = \boldsymbol{\psi}(\zeta^1, \zeta^2, z, t) = \bar{\mathbf{x}}(\zeta^1, \zeta^2, t) + z[1 + z\phi(\zeta^1, \zeta^2, t)]\mathbf{d}(\zeta^1, \zeta^2, t), \quad (19)$$

where  $\bar{\mathbf{x}}$  is the image of  $\bar{\mathbb{X}}$  on  $\mathcal{S}$ , and  $\mathbf{d}$  is a director vector along the deformed  $z$ -axis. Moreover, the scalar field  $\phi$  describes through the thickness stretching of the shell. Similar to the quantities defined on  $\mathcal{S}_0$  in Eq. (14), let  $\{\mathbf{a}_\alpha, \mathbf{a}^\alpha, a_{\alpha\beta}, a^{\alpha\beta}, \mathbf{n}, \mathbf{b}\}$  be the surface quantities defined on  $\mathcal{S}$ . It then follows that

$$\left. \begin{aligned} \mathbf{a}_\alpha &= \frac{\partial\bar{\mathbf{x}}}{\partial\zeta^\alpha}, & a_{\alpha\beta} &= \mathbf{a}_\alpha \cdot \mathbf{a}_\beta, & a^{\alpha\eta}a_{\eta\beta} &= \delta_\beta^\alpha, & \mathbf{a}^\alpha &= a^{\alpha\beta}\mathbf{a}_\beta, & \mathbf{a}_\alpha \cdot \mathbf{a}^\beta &= \delta_\alpha^\beta \\ a &= \det[a_{\alpha\beta}], & \mathbf{n} &= \frac{\mathbf{a}_1 \times \mathbf{a}_2}{|\mathbf{a}_1 \times \mathbf{a}_2|} = \frac{\mathbf{a}_1 \times \mathbf{a}_2}{\sqrt{a}}, & \mathbf{b} &= -\mathbf{n}_{,\alpha} \otimes \mathbf{a}^\alpha \end{aligned} \right\}. \quad (20)$$

Moreover, based on Eq. (19), the covariant basis vectors  $\mathbf{g}_i$  at  $\mathbf{x}$  are as follows:

$$\mathbf{g}_\alpha = \frac{\partial\mathbf{x}}{\partial\zeta^\alpha} = \mathbf{a}_\alpha + z^2\phi_{,\alpha}\mathbf{d} + z(1 + z\phi)\mathbf{d}_{,\alpha}, \quad \mathbf{g}_3 = \frac{\partial\mathbf{x}}{\partial z} = (1 + 2z\phi)\mathbf{d}. \quad (21)$$

It is observed from Eq. (21)<sub>2</sub> that the director vector  $\mathbf{d}$  and the basis vector  $\mathbf{g}_3$  are in the same direction. However, the normal vector  $\mathbf{n}$  and  $\mathbf{g}_3$  are not in the same direction, in general. Next, the vector quantities  $\mathbf{u}$  and  $\mathbf{w}$  as, respectively, the displacement field of the mid-surface and the director displacement are defined by

$$\mathbf{u} = \bar{\mathbf{x}} - \bar{\mathbb{X}} = u_i\mathbf{e}_i, \quad \mathbf{w} = \mathbf{d} - \mathbb{D} = w_i\mathbf{e}_i, \quad (22)$$

where  $u_i$  and  $w_i$  are the Cartesian components of  $\mathbf{u}$  and  $\mathbf{w}$ . The deformation gradient tensor  $\mathbf{F}$ , described in the convective coordinate system  $\{\zeta^1\zeta^2\zeta^3\}$ , takes the following form:

$$\mathbf{F} = \text{Grad}_\zeta\mathbf{x} = \frac{\partial\mathbf{x}}{\partial\zeta^i} \otimes \mathbb{G}^i = \mathbf{g}_i \otimes \mathbb{G}^i = (\mathbf{g}_i \otimes \mathbb{A}^i)\mathbf{Q}^{-1}. \quad (23)$$

In the present shell model, using Eqs. (16), (17)<sub>3</sub>, (21), and (23), and neglecting the higher-order terms involving  $z^2$ , the deformation gradient is approximated as follows:

$$\mathbf{F} \approx \tilde{\mathbf{F}}\mathbf{Q}^{-1} \quad \text{with} \quad \tilde{\mathbf{F}} = \mathbf{F}^{(0)} + z\mathbf{F}^{(1)}. \quad (24)$$

Here, the second-order tensors  $\mathbf{F}^{(0)}$  and  $\mathbf{F}^{(1)}$  are given by

$$\left. \begin{aligned} \mathbf{F}^{(0)} &= \mathbf{a}_i \otimes \mathbf{A}^i = \mathbf{a}_\alpha \otimes \mathbf{A}^\alpha + \mathbf{d} \otimes \mathbb{D} = \mathbf{I} + \text{Grad}_{\mathcal{S}_0} \mathbf{u} + \mathbf{w} \otimes \mathbb{D} \\ \mathbf{F}^{(1)} &= \mathbf{d}_{,\alpha} \otimes \mathbf{A}^\alpha + 2\phi \mathbf{d} \otimes \mathbb{D} = \text{Grad}_{\mathcal{S}_0} \mathbf{w} + 2\phi(\mathbb{D} + \mathbf{w}) \otimes \mathbb{D} - \mathbf{B} \end{aligned} \right\}, \quad (25)$$

where use has been made of Eqs. (14)<sub>8</sub> and (22). To circumvent numerical difficulties in finite element solution, the in-plane deformation gradient term  $\mathbf{F}^{(0)}$  is enhanced by the second-order tensor  $\bar{\mathbf{F}}$ , to be introduced in Section 6. Accordingly, the term  $\mathbf{F}^{(0)}$  in Eq. (24)<sub>2</sub> is replaced by  $\mathbf{F}^{(0)} + \bar{\mathbf{F}}$ . Moreover, following Ramezani and Naghadabadi [73] in the context of the micropolar Timoshenko beam model, it is assumed that the micro-rotation pseudo-vector is constant along the shell thickness, namely  $\boldsymbol{\theta} = \tilde{\boldsymbol{\theta}}(\zeta^1, \zeta^2)$ . Accordingly, the micro-rotation tensor  $\tilde{\mathbf{R}}(\boldsymbol{\theta})$  is independent of the  $z$  coordinate. Keeping this in mind and using Eqs. (5)<sub>1</sub>, (6)<sub>1</sub>, (17)<sub>3</sub>, (18)<sub>2</sub>, and (24), the micropolar deformation measures  $\tilde{\mathbf{U}}$  and  $\boldsymbol{\Gamma}$ , in the present shell formulation, may be written as

$$\tilde{\mathbf{U}} = \tilde{\mathbf{R}}^\top \mathbf{F}^* \mathbf{Q}^{-1} = \tilde{\mathbf{R}}^\top (\mathbf{F}^{(0)} + \bar{\mathbf{F}} + z\mathbf{F}^{(1)}) \mathbf{Q}^{-1}, \quad \boldsymbol{\Gamma} = -\frac{1}{2} \boldsymbol{\mathcal{E}} : [\tilde{\mathbf{R}}^\top (\text{Grad}_{\mathcal{S}_0} \tilde{\mathbf{R}}) \mathbf{Q}^{-1}]. \quad (26)$$

where  $\mathbf{F}^* = \tilde{\mathbf{F}} + \bar{\mathbf{F}}$  is the enhanced form of  $\tilde{\mathbf{F}}$ . The present formulation with  $\{\mathbf{u}, \mathbf{w}, \phi, \boldsymbol{\theta}\}$  as the unknown field variables may be regarded as a 10-parameter micropolar shell model. In other words, the present formulation is the extension of the classical 7-parameter shell model, with  $\{\mathbf{u}, \mathbf{w}, \phi\}$  as its unknowns, introduced by Sansour (e.g., [66, 67]).

## 5. Variational formulation

In this section, the virtual work statement of the problem is presented. The principle of virtual work is based on the requirement that  $\delta\mathcal{U} - \delta\mathcal{W} = 0$ , where  $\delta\mathcal{U}$  and  $\delta\mathcal{W}$  are the virtual internal energy and the virtual work of external loads, respectively [74]. Let  $\delta\Psi$  and  $\delta\hat{\mathcal{W}}$  denote, respectively,  $\delta\mathcal{U}$  and  $\delta\mathcal{W}$  per unit reference volume. In what follows, the expressions for  $\delta\Psi$  and  $\delta\hat{\mathcal{W}}$  in the present formulation are derived. Moreover, for the linearization purpose to be used in the next section, the increments of  $\delta\Psi$  and  $\delta\hat{\mathcal{W}}$  are also calculated.

In the sequel, it is assumed that the material is hyperelastic, and thermal effects are also neglected. Accordingly, the internal energy density per unit reference volume is of the form  $\Psi = \bar{\Psi}(\tilde{\mathbf{U}}, \mathbf{\Gamma}) = \tilde{\Psi}(\tilde{\mathbf{V}}, \gamma)$  [42, 46]. In particular, from the dependency of  $\Psi$  to the material tensors  $\tilde{\mathbf{U}}$  and  $\mathbf{\Gamma}$  it follows that

$$\delta\Psi = \frac{\partial\Psi}{\partial\tilde{\mathbf{U}}}: \delta\tilde{\mathbf{U}} + \frac{\partial\Psi}{\partial\mathbf{\Gamma}}: \delta\mathbf{\Gamma} = (\tilde{\mathbf{R}} \frac{\partial\Psi}{\partial\tilde{\mathbf{U}}} \mathbf{F}^\top): (\delta\mathbf{Y} - \delta\hat{\omega}) + (\tilde{\mathbf{R}} \frac{\partial\Psi}{\partial\mathbf{\Gamma}} \mathbf{F}^\top): \text{grad} \delta\omega, \quad (27)$$

where use has been made of Eq. (7). Moreover, the constitutive relations for the various stress and couple stress measures are as follows [32]:

$$\{\tilde{\mathbf{P}}, \tilde{\mathbf{M}}\} = \left\{ \frac{\partial\Psi}{\partial\tilde{\mathbf{U}}}, \frac{\partial\Psi}{\partial\mathbf{\Gamma}} \right\}, \quad \{\mathbf{P}, \mathbf{M}\} = \tilde{\mathbf{R}} \left\{ \frac{\partial\Psi}{\partial\tilde{\mathbf{U}}}, \frac{\partial\Psi}{\partial\mathbf{\Gamma}} \right\}, \quad \{\boldsymbol{\sigma}, \mathbf{m}\} = \frac{1}{J} \tilde{\mathbf{R}} \left\{ \frac{\partial\Psi}{\partial\tilde{\mathbf{U}}}, \frac{\partial\Psi}{\partial\mathbf{\Gamma}} \right\} \mathbf{F}^\top. \quad (28)$$

It is noted that Eqs. (27) and (28) hold for all three-dimensional micropolar hyperelastic solids. For the present shell model, first the quantities denoted by  $\delta\boldsymbol{\Upsilon}^{(1)}$  and  $\delta\boldsymbol{\Upsilon}^{(2)}$  are defined by

$$\left. \begin{aligned} \delta\boldsymbol{\Upsilon}^{(1)} &= \tilde{\mathbf{R}}\delta\tilde{\mathbf{U}}\mathbf{Q} = \delta\mathbf{F}^{(0)} + \delta\bar{\mathbf{F}} + z\delta\mathbf{F}^{(1)} - \delta\hat{\omega}\mathbf{F}^* \\ \delta\boldsymbol{\Upsilon}^{(2)} &= \tilde{\mathbf{R}}\delta\mathbf{\Gamma}\mathbf{Q} = (\text{Grad}\delta\omega)\mathbf{Q} = \text{Grad}_{S_0}\delta\omega \end{aligned} \right\}. \quad (29)$$

Next, after replacing  $\tilde{\mathbf{F}}$  by the enhanced form  $\mathbf{F}^*$ , combination of Eqs. (26), (27)<sub>1</sub>, (28)<sub>1,2</sub>, and (29) leads to the following expression for  $\delta\Psi$ :

$$\delta\Psi = \mathbf{P}^{(0)}: \delta\boldsymbol{\Upsilon}^{(1)} + \mathbf{M}^{(0)}: \delta\boldsymbol{\Upsilon}^{(2)} \quad \text{with} \quad \{\mathbf{P}^{(0)}, \mathbf{M}^{(0)}\} = \{\mathbf{P}\mathbf{Q}^{-1}, \mathbf{M}\mathbf{Q}^{-1}\}. \quad (30)$$

For linearization purpose, the increment of  $\delta\Psi$  under the increment of the field variables  $\Delta\mathbf{u}$ ,  $\Delta\mathbf{w}$ ,  $\Delta\phi$ , and  $\Delta\boldsymbol{\theta}$  is needed. Accordingly, from Eqs. (27)<sub>1</sub> and (30) it follows that

$$\begin{aligned} \Delta\delta\Psi &= \delta\boldsymbol{\Upsilon}^{(1)}: \boldsymbol{\mathcal{C}}^{(1)}: \Delta\boldsymbol{\Upsilon}^{(1)} + \delta\boldsymbol{\Upsilon}^{(2)}: \boldsymbol{\mathcal{C}}^{(2)}: \Delta\boldsymbol{\Upsilon}^{(2)} + \delta\boldsymbol{\Upsilon}^{(1)}: \boldsymbol{\mathcal{C}}^{(3)}: \Delta\boldsymbol{\Upsilon}^{(2)} \\ &\quad + \delta\boldsymbol{\Upsilon}^{(2)}: \boldsymbol{\mathcal{C}}^{(4)}: \Delta\boldsymbol{\Upsilon}^{(1)} + \mathbf{P}^{(0)}: \Delta\delta\mathbf{H}^{(1)} + \mathbf{M}^{(0)}: \Delta\delta\mathbf{H}^{(2)}, \end{aligned} \quad (31)$$

where  $\Delta\delta\mathbf{H}^{(1)}$  and  $\Delta\delta\mathbf{H}^{(2)}$  are as follows:

$$\left. \begin{aligned} \Delta\delta\mathbf{H}^{(1)} &= \frac{1}{2}(\Delta\hat{\omega}\delta\hat{\omega} + \delta\hat{\omega}\Delta\hat{\omega})\mathbf{F}^* - (\delta\hat{\omega}\Delta\mathbf{F}^* + \Delta\hat{\omega}\delta\mathbf{F}^*) \\ \Delta\delta\mathbf{H}^{(2)} &= -\frac{1}{2}(\Delta\hat{\omega}\text{Grad}_{S_0}\delta\omega + \delta\hat{\omega}\text{Grad}_{S_0}\Delta\omega) \end{aligned} \right\}. \quad (32)$$

Moreover, the fourth-order tensors  $\boldsymbol{\mathcal{C}}^{(\mathcal{I})}$  ( $\mathcal{I} = 1, 2, 3, 4$ ) have the following components:

$$\mathcal{C}_{ijkl}^{(\mathcal{I})} = \tilde{R}_{iP}\tilde{R}_{kQ}Q_{JR}^{-1}Q_{LS}^{-1}\tilde{\mathcal{C}}_{PQRS}^{(\mathcal{I})} \quad \text{with} \quad Q_{JR}^{-1} = (\mathbf{Q}^{-1})_{JR}, \quad (33)$$

and  $\tilde{\mathcal{C}}_{PJKL}^{(\mathcal{I})}$  are the components of the following fourth-order tensors:

$$\{\tilde{\mathcal{C}}^{(1)}, \tilde{\mathcal{C}}^{(2)}, \tilde{\mathcal{C}}^{(3)}, \tilde{\mathcal{C}}^{(4)}\} = \left\{ \frac{\partial^2 \Psi}{\partial \tilde{\mathbf{U}} \partial \tilde{\mathbf{U}}}, \frac{\partial^2 \Psi}{\partial \mathbf{\Gamma} \partial \mathbf{\Gamma}}, \frac{\partial^2 \Psi}{\partial \tilde{\mathbf{U}} \partial \mathbf{\Gamma}}, \frac{\partial^2 \Psi}{\partial \mathbf{\Gamma} \partial \tilde{\mathbf{U}}} \right\}. \quad (34)$$

In this work, a micropolar neo-Hookean constitutive model of the form proposed in Ref. [32] is employed, according to which the free energy per unit reference volume is given by

$$\Psi = (\eta + \frac{1}{2}\mu) \text{tr}(\tilde{\mathbf{U}}\tilde{\mathbf{U}}^\top) - \eta \text{tr}(\tilde{\mathbf{U}}^2) + \frac{1}{2}\lambda(\ln J)^2 - \mu \ln J + \frac{1}{2}\mu l^2 \text{tr}(\mathbf{\Gamma}\mathbf{\Gamma}^\top), \quad (35)$$

where  $\eta$  is a material constant, and  $l$  is a length-scale parameter. From Eqs. (28)<sub>1</sub> and (35), the material stress  $\tilde{\mathbf{P}}$  and the couple stress  $\tilde{\mathbf{M}}$  are then calculated to be

$$\tilde{\mathbf{P}} = (\mu + \eta)\tilde{\mathbf{U}} - \eta\tilde{\mathbf{U}}^\top + (\lambda \ln J - \mu)\tilde{\mathbf{U}}^{-\top}, \quad \tilde{\mathbf{M}} = \mu l^2 \mathbf{\Gamma}. \quad (36)$$

Moreover, Eqs. (34) and (35) lead to the following fourth-order tensors  $\tilde{\mathcal{C}}^{(\mathcal{I})}$  ( $\mathcal{I} = 1, 2, 3, 4$ ):

$$\left. \begin{aligned} \tilde{\mathcal{C}}^{(1)} &= (\mu + \eta)\mathbf{I} \odot \mathbf{I} - \eta\mathbf{I} \boxtimes \mathbf{I} + \lambda\tilde{\mathbf{U}}^{-\top} \otimes \tilde{\mathbf{U}}^{-\top} + (\mu - \lambda \ln J)\tilde{\mathbf{U}}^{-\top} \boxtimes \tilde{\mathbf{U}}^{-\top} \\ \tilde{\mathcal{C}}^{(2)} &= \mu l^2 \mathbf{I} \odot \mathbf{I}, \quad \tilde{\mathcal{C}}^{(3)} = \tilde{\mathcal{C}}^{(4)} = \mathbf{0} \end{aligned} \right\}. \quad (37)$$

Next, it is recalled that  $\mathbb{B}^{\text{ext}}$  exerts the body couple per unit reference volume  $\mathbb{p}^*$  on an HMSM, as given by Eq. (12)<sub>2</sub>. Noting that  $\mathbb{p}^*$  is work-conjugate to the micro-rotation  $\boldsymbol{\theta}$ , the virtual work per unit reference volume  $\delta\hat{\mathcal{W}}$  expended by  $\mathbb{B}^{\text{ext}}$  on an HMSM is given by

$$\delta\hat{\mathcal{W}} = \mathbb{p}^* \cdot \delta\boldsymbol{\theta} = \frac{1}{\mu_0} [(\mathbf{F}\tilde{\mathbb{B}}^{\text{rem}}) \times \mathbb{B}^{\text{ext}}] \cdot \delta\boldsymbol{\theta}. \quad (38)$$

For the linearization purpose, the increment of  $\delta\hat{\mathcal{W}}$  takes the following form:

$$\Delta\delta\hat{\mathcal{W}} = \frac{1}{\mu_0} [(\Delta\mathbf{F}^* \mathbf{Q}^{-1} \tilde{\mathbb{B}}^{\text{rem}}) \times \mathbb{B}^{\text{ext}}] \cdot \delta\boldsymbol{\theta}, \quad (39)$$

which leads to the expression for the load stiffness matrix in the next section.

## 6. Finite element formulation

In this section, a nonlinear finite element formulation in the material framework is developed. Let  $\mathcal{S}_0^{\mathfrak{e}}$  be a typical element in the referential midsurface  $\mathcal{S}_0^{\mathfrak{e}}$ . To perform numerical integration, the typical element is mapped to the two-dimensional parent square element  $\square = [-1, 1] \times [-1, 1]$

in the  $\{\xi, \eta\}$  space, with  $\xi, \eta \in [-1, 1]$ . The field variables  $\{u_i, w_i, \theta_i, \phi\}$ , over the parent element  $\mathcal{S}_0^s$ , are interpolated as follows:

$$u_i = \mathbf{N}_u \mathbf{U}_i, \quad w_i = \mathbf{N}_w \mathbf{W}_i, \quad \theta_i = \mathbf{N}_\theta \mathbf{\Theta}_i, \quad \phi = \mathbf{N}_\phi \mathbf{\Phi}, \quad (40)$$

where  $\mathbf{N}_u = \{N_u^1, N_u^2, \dots, N_u^{n_u}\}$  is a row vector containing the shape functions that interpolate the midsurface displacement  $u_i$  over the element. Here,  $n_u$  is the number of nodes of the element that possess the  $u_i$ -DOF. Let  $U_i^{\mathcal{I}}$  be the displacement component  $u_i$  at the  $\mathcal{I}$ 'th node ( $\mathcal{I} = 1, 2, \dots, n_u$ ) of the element. Accordingly,  $\mathbf{U}_i = \{U_i^1, U_i^2, \dots, U_i^{n_u}\}^\top$  is a column vector that involves all  $U_i^{\mathcal{I}}$ 's over the element. Similar definitions hold for the other quantities in Eq. (40). Moreover, similar relations hold for the increment  $\{\Delta u_i, \Delta w_i, \Delta \theta_i, \Delta \phi\}$  and variation  $\{\delta u_i, \delta w_i, \delta \theta_i, \delta \phi\}$  of the field variables. The generalized displacement vector  $\mathbf{v}^e$  involving all nodal DOFs of the typical element may be written as

$$\mathbf{v}_{n^e \times 1}^e = \{\mathbf{U}_1^\top, \mathbf{U}_2^\top, \mathbf{U}_3^\top, \mathbf{W}_1^\top, \mathbf{W}_2^\top, \mathbf{W}_3^\top, \mathbf{\Theta}_1^\top, \mathbf{\Theta}_2^\top, \mathbf{\Theta}_3^\top, \mathbf{\Phi}^\top\}^\top, \quad (41)$$

where  $n^e = 3(n^u + n^w + n^\theta) + n^\phi$  is the number of nodal DOFs. Based on Esq. (2), (25), (29), and (40), the following relations hold:

$$\left. \begin{aligned} \delta F_{iJ}^{(0)} &= A^{*\alpha J} \mathbf{N}_{u,\alpha} \delta \mathbf{U}_i + \mathbf{N}_w D_J \delta \mathbf{W}_i = \mathbf{b}_{iJ}^{(0)} \delta \mathbf{v}^e \\ \delta F_{iJ}^{(1)} &= (A^{*\alpha J} \mathbf{N}_{w,\alpha} + 2\phi D_J \mathbf{N}_w) \delta \mathbf{W}_i + 2d_i D_J \mathbf{N}_\phi \delta \mathbf{\Phi} = \mathbf{b}_{iJ}^{(1)} \delta \mathbf{v}^e \\ (\delta \hat{\omega} \mathbf{F}^*)_{iJ} &= \epsilon_{ijk} \Lambda_{kp} F_{jJ}^* \mathbf{N}_\theta \delta \mathbf{\Theta}_p = \mathbf{b}_{iJ}^{(\omega F)} \delta \mathbf{v}^e \\ \delta Y_{iJ}^{(2)} &= A^{*\alpha J} (\Lambda_{ip} \mathbf{N}_\theta)_{,\alpha} \delta \mathbf{\Theta}_p = \mathbf{b}_{iJ}^{(2)} \delta \mathbf{v}^e \end{aligned} \right\}. \quad (42)$$

Here, the last equality in each relation indicates that all components can be expressed in terms of the generalized virtual displacement vector  $\delta \mathbf{v}^e$ . Next, the enhanced deformation gradient tensor  $\bar{\mathbf{F}}$  is considered. Let  $\boldsymbol{\alpha} = \{\alpha_1, \alpha_2, \dots, \alpha_{\mathcal{P}^*}\}^\top$  be the column vector of enhanced parameters  $\alpha_{\mathcal{P}}$ 's ( $\mathcal{P} = 1, 2, \dots, \mathcal{P}^*$ ), where  $\mathcal{P}^*$  is the total number of enhanced parameters. The components of  $\bar{\mathbf{F}}$  and its variation/increment depend linearly on  $\alpha_{\mathcal{P}}$ 's (see, e.g., Refs. [68–71]). Here, following the notation used in Eq. (42), one may write

$$\{\bar{F}_{iJ}, \delta \bar{F}_{iJ}, \Delta \bar{F}_{iJ}\} = \bar{\mathbf{b}}_{iJ} \{\boldsymbol{\alpha}, \delta \boldsymbol{\alpha}, \Delta \boldsymbol{\alpha}\} \quad \text{or} \quad \{\bar{\mathbf{F}}, \delta \bar{\mathbf{F}}, \Delta \bar{\mathbf{F}}\} = \bar{\mathbf{B}} \{\boldsymbol{\alpha}, \delta \boldsymbol{\alpha}, \Delta \boldsymbol{\alpha}\}, \quad (43)$$

where  $\bar{\mathbf{b}}_{iJ}$  are the  $\mathcal{P}^* \times 1$  row vectors,  $\bar{\mathbf{F}}$  is the  $9 \times 1$  vectorial representation of  $\bar{\mathbf{F}}$ , and  $\bar{\mathbf{B}}$  is a  $9 \times \mathcal{P}^*$  matrix the rows of which are  $\bar{\mathbf{b}}_{iJ}$ .

Now, let  $\mathbb{B}^{(\mathcal{N})}$  ( $\mathcal{N} = 0, 1, 2$ ) and  $\mathbb{B}^{(\omega F)}$  be the  $9 \times n^e$  matrices whose rows are  $\mathbb{b}_{iJ}^{(\mathcal{N})}$  and  $\mathbb{b}_{iJ}^{(\omega F)}$ , respectively. From Eqs. (29), (42), and (43) it then follows that

$$\delta \mathbb{Y}^{(1)} = \tilde{\mathbb{B}} \delta \mathbb{v} + \bar{\mathbb{B}} \delta \boldsymbol{\alpha} \quad \text{and} \quad \delta \mathbb{Y}^{(2)} = \mathbb{B}^{(2)} \delta \mathbb{v} \quad \text{with} \quad \tilde{\mathbb{B}} = \mathbb{B}^{(0)} + \mathbb{B}^{(\omega F)} + z \mathbb{B}^{(1)}. \quad (44)$$

The differential volume element  $d\mathcal{V}_0^e$  located at the elevation  $z$  with respect to the typical element  $\mathcal{S}_0^e$  is given by (e.g., [66])

$$d\mathcal{V}_0^e = Q d\mathcal{S}_0^e dz \quad \text{with} \quad Q = \det \mathbf{Q} \quad \text{and} \quad d\mathcal{S}_0^e = \sqrt{A} d\zeta^1 d\zeta^2. \quad (45)$$

By integrating Eqs. (30) and (38) over the reference volume, the virtual internal energy of the element,  $\delta \mathcal{U}^e = \int_{\mathcal{V}_0^e} \Psi d\mathcal{V}_0^e$ , and the virtual work of external magnetic loading on the element,  $\delta \mathcal{W}^e = \int_{\mathcal{V}_0^e} \hat{\mathcal{W}} d\mathcal{V}_0^e$ , are obtained. Using Eqs. (29) and (44), the expressions for  $\delta \mathcal{U}^e$  and  $\delta \mathcal{W}^e$  may be written as

$$\delta \mathcal{U}^e = \delta \mathbb{v}^\top \mathbb{F}_{\text{int}}^v + \delta \boldsymbol{\alpha}^\top \mathbb{F}_{\text{int}}^\alpha, \quad \delta \mathcal{W}^e = \delta \boldsymbol{\Theta}_i^\top \mathbb{F}_{\text{ext}i}^\theta = \delta \mathbb{v}^\top \mathbb{F}_{\text{ext}}^v, \quad (46)$$

where the internal force vectors  $\mathbb{F}^{\text{int}v}$  and  $\mathbb{F}^{\text{int}\alpha}$  are as follows:

$$\mathbb{F}_{\text{int}}^v = \int_{\mathcal{V}_0^e} (\tilde{\mathbb{B}}^\top \mathbb{P}^{(0)} + \mathbb{B}^{(2)\top} \mathbb{M}^{(0)}) d\mathcal{V}_0^e, \quad \mathbb{F}_{\text{int}}^\alpha = \int_{\mathcal{V}_0^e} \bar{\mathbb{B}}^\top \mathbb{P}^{(0)} d\mathcal{V}_0^e. \quad (47)$$

Moreover, the external force vector  $\mathbb{F}_{\text{ext}i}^\theta$ , work conjugate to  $\boldsymbol{\Theta}_i$ , is given by

$$\mathbb{F}_{\text{ext}i}^\theta = \frac{1}{\mu_0} \int_{V_0^e} \epsilon_{imj} F_{mJ} \tilde{B}_J^{\text{rem}} B_j^{\text{ext}} \mathbf{N}_\theta^\top d\mathcal{V}_0^e. \quad (48)$$

Next, the linearized equations resulting from Eqs. (31), (39), and (46) may be written as

$$\Delta \delta \mathcal{U}^e - \Delta \delta \mathcal{W}^e = -(\delta \mathcal{U}^e - \delta \mathcal{W}^e), \quad (49)$$

from which the following system of algebraic equations is extracted:

$$\begin{bmatrix} \mathbb{K}_{\text{mat}}^{vv} + \mathbb{K}_{\text{geo}}^{vv} - \mathbb{K}_{\text{load}}^{vv} & \mathbb{K}_{\text{mat}}^{v\alpha} + \mathbb{K}_{\text{geo}}^{v\alpha} - \mathbb{K}_{\text{load}}^{v\alpha} \\ \mathbb{K}_{\text{mat}}^{v\alpha\top} + \mathbb{K}_{\text{geo}}^{v\alpha} & \mathbb{K}_{\text{mat}}^{\alpha\alpha} \end{bmatrix} \begin{Bmatrix} \Delta \mathbb{v} \\ \Delta \boldsymbol{\alpha} \end{Bmatrix} = - \begin{Bmatrix} \mathbb{F}_{\text{int}}^v - \mathbb{F}_{\text{ext}}^v \\ \mathbb{F}_{\text{int}}^\alpha \end{Bmatrix}, \quad (50)$$

where the subscripts "mat", "geo", and "load", represent the material, geometric, and load part of the element stiffness matrix. In particular, the material sub-matrices  $\mathbb{K}_{\text{mat}}^{vv}$ ,  $\mathbb{K}_{\text{mat}}^{v\alpha}$ , and  $\mathbb{K}_{\text{mat}}^{\alpha\alpha}$  in Eq. (50) are as follows:

$$\left. \begin{aligned} \mathbb{K}_{\text{mat}}^{vv} &= \int_{V_0^e} [\tilde{\mathbb{B}}^\top (\mathbb{A}^{(1)} \tilde{\mathbb{B}} + \mathbb{A}^{(3)} \mathbb{B}^{(2)}) + \mathbb{B}^{(2)\top} (\mathbb{A}^{(2)} \mathbb{B}^{(2)} + \mathbb{A}^{(4)} \tilde{\mathbb{B}})] d\mathcal{V}_0^e \\ \mathbb{K}_{\text{mat}}^{v\alpha} &= \int_{V_0^e} (\tilde{\mathbb{B}}^\top \mathbb{A}^{(1)} + \mathbb{B}^{(2)\top} \mathbb{A}^{(4)}) \bar{\mathbb{B}} d\mathcal{V}_0^e, \quad \mathbb{K}_{\text{mat}}^{\alpha\alpha} = \int_{V_0^e} \bar{\mathbb{B}}^\top \mathbb{A}^{(1)} \bar{\mathbb{B}} d\mathcal{V}_0^e \end{aligned} \right\}. \quad (51)$$

Moreover, the load sub-matrices  $\mathbb{K}_{\text{load}}^{vv}$ ,  $\mathbb{K}_{\text{load}}^{v\alpha}$  are given by

$$\left. \begin{aligned} \mathbb{K}_{\text{load}}^{vv} &= \int_{V_0^e} \epsilon_{ijk} Q_{JN}^{-1} \tilde{B}_N^{\text{rem}} B_j^{\text{ext}} \mathbf{y}_k (\mathbf{b}_{iJ}^{(0)} + z \mathbf{b}_{iJ}^{(1)}) d\mathcal{V}_0^e \\ \mathbb{K}_{\text{load}}^{v\alpha} &= \int_{V_0^e} \epsilon_{ijk} Q_{JN}^{-1} \tilde{B}_N^{\text{rem}} B_j^{\text{ext}} \mathbf{y}_k \bar{\mathbf{b}}_{iJ} d\mathcal{V}_0^e \end{aligned} \right\}, \quad (52)$$

where  $\mathbf{y}_k = \{\mathbf{0}_{1 \times 3(n^u + n^w)}, \mathbf{0}_{1 \times (k-1)n^\theta}, \mathbb{N}_\theta, \mathbf{0}_{1 \times (3-k)n^\theta}, \mathbf{0}_{1 \times n^\phi}\}^\top$ , with  $k \in \{1, 2, 3\}$ , is a column vector whose nonzero entry is  $\mathbb{N}_\theta$ . The expressions for the geometric sub-matrices, resulting from the term  $\mathbf{P}^{(0)} : \Delta \delta \mathbf{H}^{(1)} + \mathbf{M}^{(0)} : \Delta \delta \mathbf{H}^{(2)}$  in Eq. (31), are too lengthy and are not presented here. Finally, the assembled system of equations may be written of the form  $\tilde{\mathbb{K}} \Delta \tilde{\mathbf{V}} = -\tilde{\mathbb{R}}$ . In this relation,  $\Delta \tilde{\mathbf{V}}$  is the incremental generalized displacement vector that contains all nodal DOFs,  $\tilde{\mathbb{K}}$  is the assembled stiffness matrix, and  $\tilde{\mathbb{R}}$  is the assembled residual vector. After finding  $\Delta \tilde{\mathbf{V}}$ , the non-rotational quantities are update via the relations  $\mathbf{u} + \Delta \mathbf{u} \rightarrow \mathbf{u}$ ,  $\mathbf{w} + \Delta \mathbf{w} \rightarrow \mathbf{w}$ , and  $\phi + \Delta \phi \rightarrow \phi$ . However, the update procedure for the rotation pseudo-vector is completely different. Let  $\Delta \boldsymbol{\theta}$  be the increment of the rotation pseudo-vector. The updated rotation pseudo-vector resulting from the two subsequent rotations  $\boldsymbol{\theta}$  and  $\Delta \boldsymbol{\theta}$  is then calculated via the following relations [75]:

$$\boldsymbol{\theta}_{\text{updated}}^* = \frac{\boldsymbol{\theta}^* + \Delta \boldsymbol{\theta}^* + (\Delta \hat{\boldsymbol{\theta}}^*) \boldsymbol{\theta}^*}{1 - \boldsymbol{\theta}^* \cdot \Delta \boldsymbol{\theta}^*} \quad \text{with} \quad \boldsymbol{\theta}^* = \frac{\boldsymbol{\theta}}{\theta} \tan \frac{\theta}{2}. \quad (53)$$

It is noted that  $\boldsymbol{\theta}^*$  is the normalized rotation pseudo-vector. Moreover,  $\Delta \hat{\boldsymbol{\theta}}^*$  is the skew-symmetric tensor corresponding to  $\Delta \boldsymbol{\theta}^*$ . The proof of Eq. (53) is lengthy and is available in, e.g., Argyris [75].

## 7. Numerical examples

To examine the applicability and performance of the developed formulation, several numerical examples are provided in this section. To do so, a home-written FE code based on the formulation presented in the previous sections has been prepared. The 10-parameter micropolar shell element designed for the present numerical simulations is an eight-node quadrilateral. All eight nodes contain the three displacement components  $u_i$ . However, only the corner nodes contain the  $w_i$ ,  $\phi$ , and  $\theta_i$  DOFs. In other words, the DOF parameters defined after Eqs. (40) and (41) are  $n^u = 8$  and  $n^w = n^\theta = n^\phi = 4$ . Following Korelc and Wriggers [70], the enhancing deformation gradient  $\bar{\mathbf{F}}$  is considered to be of the following form:

$$\bar{\mathbf{F}} = \mathbf{J}^{-\top} \bar{\mathbf{F}}^{\text{ref}} \mathbf{J}^{-1}, \quad (54)$$

where  $\mathbf{J}$  is the Jacobi matrix between the physical and parent elements. Moreover,  $\bar{\mathbf{F}}^{\text{ref}}$  is the enhancing deformation gradient defined in the parent  $\{\xi, \eta\}$  space. In this work, the nonzero components of  $\bar{\mathbf{F}}^{\text{ref}}$  are considered as follows:

$$\bar{F}_{13}^{\text{ref}} = \alpha_1\xi + \alpha_2\eta, \quad \bar{F}_{23}^{\text{ref}} = \alpha_3\xi + \alpha_4\eta, \quad \bar{F}_{33}^{\text{ref}} = \alpha_5\xi + \alpha_6\eta, \quad (55)$$

which are linear functions in terms of the parent coordinates  $\xi$  and  $\eta$ . This indicates that  $\bar{\mathbf{F}}$  contains six enhanced parameters, namely  $\mathcal{P}^* = 6^1$ . The standard  $2 \times 2$  Gauss–Legendre integration rule has been employed to evaluate all integrals over the element surface. Moreover, the two-point rule has been used for integration along the shell thickness.

### 7.1. VERIFICATION EXAMPLE: bending of beam-like strips

To examine the validity of the results of the proposed formulation, the flexural deformation of four beam-like strips, made of HMSMs and subject to an external magnetic flux is studied in this example. Extensive experiments on these structures have been previously conducted by Zhao et al. [24]. The mechanical properties of the material are  $\mu = 303$  and  $\lambda = 7300$  (kPa). The referential residual magnetic flux density is along the undeformed centreline and its magnitude is  $|\tilde{\mathbb{B}}^{\text{rem}}| = 143$  (mT). The width of all strips is 5 mm, and their lengths and heights are given by the sets  $L \in \{11, 19.2, 17.2, 17.2\}$  (mm) and  $h \in \{1.1, 1.1, 0.84, 0.42\}$  (mm), respectively. The aspect ratio parameter is defined by "AR = L/h". For the given data, the aspect ratios of the strips are 10, 17.5, 20.5, and 41, respectively. The strips are clamped at  $X_1 = 0$ , and are subjected to the maximum external magnetic flux  $\mathbb{B}_{\text{max}}^{\text{ext}} = 50\mathbf{e}_3$  (mT).

Convergence analysis reveals that the minimum required number of elements along the length of the strips is 10, 15, 30, and 40, respectively. Additionally, two elements in the width direction are necessary for the four strips. Furthermore, for  $\eta = 0.1\mu$  and  $l = 0.1h$ , the results of the present formulation will be very close to the available data reported in [24]. These relations will be also used for all simulations presented in this work.

The nondimensional tip deflection  $u_3^T/L$  versus the load parameter  $\frac{10^3}{\mu\mu_0}|\mathbb{B}^{\text{ext}}||\tilde{\mathbb{B}}^{\text{rem}}|$  is depicted in Fig. 2(a). It is observed that the present results are in good agreement with the experimental

---

<sup>1</sup>It is also possible to include the nonlinear terms involving  $\{\xi^2, \eta^2, \xi\eta^2, \xi^2\eta\}$  or  $\{1-3\xi^2, 1-3\eta^2, \xi(1-3\eta^2), \eta(1-3\xi^2)\}$  in the components of  $\bar{\mathbf{F}}^{\text{ref}}$ . In this case, the number of the enhanced parameters increases from 6 to 39. However, our numerical simulations reveal that the change in the results is negligible.



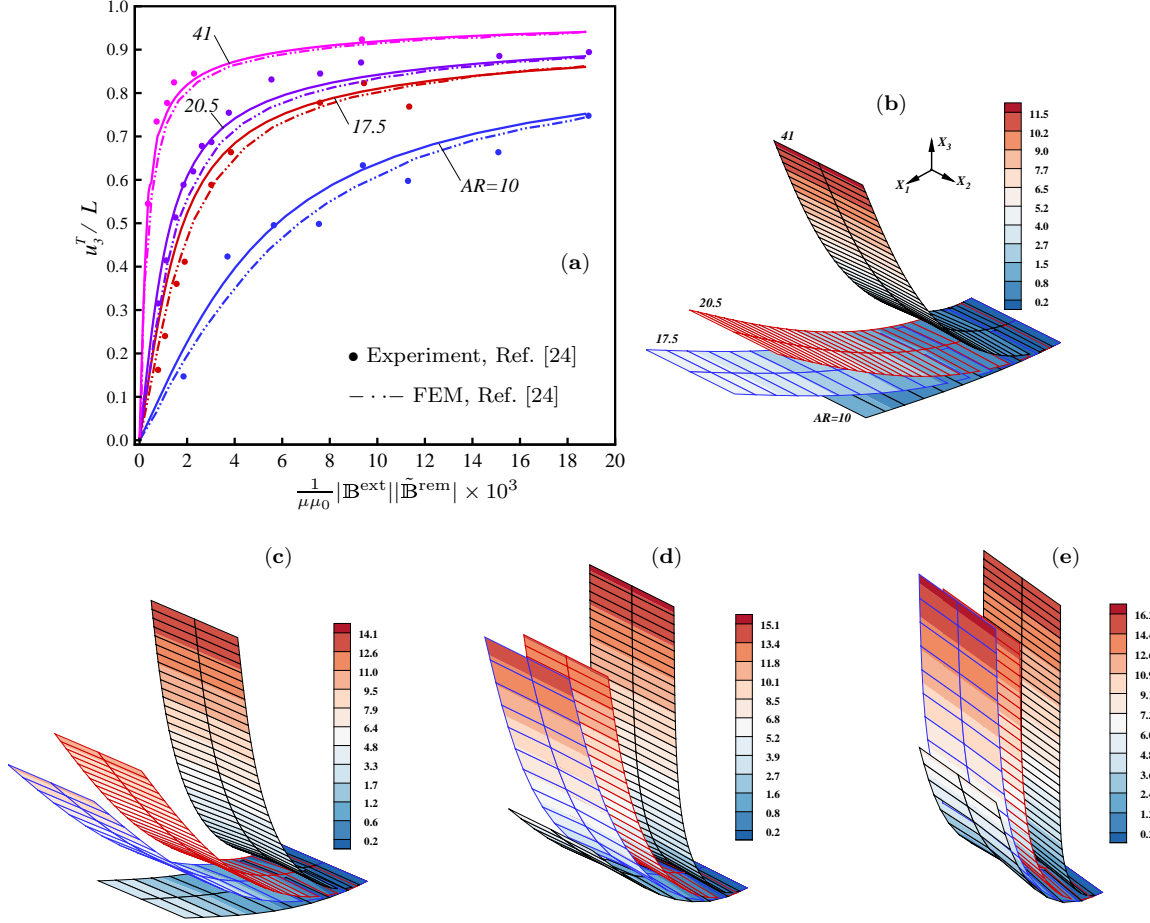


Figure 2: Beam-like strips under magnetic loading, (a): load-deflection curves, (b,c,d,e): deformed shapes with the contour plots of  $u_3$  (in mm) for  $|\mathbb{B}^{\text{ext}}| \in \{2, 5, 15, 50\}$  (mT)

and numerical data obtained by Zhao et al. [24]. The deformed shapes of the strips for four values of the external magnetic flux are displayed in Figs. 2(b,c,d,e). To have a comparison between the deformation of the strips for a specific value of  $|\mathbb{B}^{\text{ext}}|$ , the four strips are plotted in the same figure. In particular, from Fig. 2(b) it is observed that the slender strip with  $AR = 41$  exhibits very large deformations even for small values of  $|\mathbb{B}^{\text{ext}}|$ .

### 7.2. Deformation of a hollow cross

In this example, the large deformation of a hollow cross under magnetic loading is investigated. This example has been previously studied by Kim et al. [18] and Zhao et al. [24]. As shown in Fig. 3(a), the geometry is composed of 24 trapezoidal blocks. The block dimensions in the  $X_1X_2$  plane are displayed in the figure, and its thickness is 0.41 mm. The mechanical

properties are the same as those in the previous example, namely  $\mu = 303$  and  $\lambda = 7300$  (kPa). The magnitude of the referential remnant magnetic flux density is  $|\tilde{\mathbb{B}}^r| = 102$  (mT). As shown on Fig. 3(a), the direction of  $\tilde{\mathbb{B}}^r$  is constant in each block, but varies in different blocks. The maximum external magnetic flux density  $\mathbb{B}_{\max}^{\text{ext}} = -200\mathbf{e}_3$  (mT) is applied to the body. Due to symmetry in the  $X_1X_2$  plane, it is sufficient to discretize merely one-quarter of the geometry.

Numerical simulations reveal that a mesh of  $6 \times 6$  elements in each trapezoidal block leads to convergent results. Variations of the displacement component  $u_3$  for several material points versus the nondimensional loading parameter  $\frac{10^3}{\mu\mu_0}|\mathbb{B}^{\text{ext}}||\tilde{\mathbb{B}}^{\text{rem}}|$  are depicted in Fig. 3(a). It is noted that the lateral deflection at the material points  $A$  and  $G$  is considered to be zero. At the final stage of deformation, the lateral displacement at the points  $E$  and  $C$  is very close to each other. More precisely, the maximum lateral displacement of about 10.39 mm at the material point  $C$  is observed. The final deformed shape of the body observed in the experiments of Kim et al. [18] is illustrated in Fig. 3(b). Moreover, the deformed shapes of the hollow cross under four different values of the external magnetic flux are displayed in Figs. 3(c,d,e,f). By comparing figures 3(b) and 3(e), it is deduced that the final deformed shape obtained by the present formulation is qualitatively similar to that reported in the experimental studies of Kim et al. [18].

### 7.3. Deformation of a cross-shaped geometry

In this example, the finite elastic deformation of a cross-shaped thin body made of HMSMs is studied. As shown in Fig. 4(a), the geometry is composed of nine equal blocks. The block dimensions in the  $X_1X_2$  plane are  $6 \times 6$  (mm), and its thickness is 0.9 (mm). The blocks are welded together by a specific procedure advocated in Kuang et al. [20]. The mechanical properties are considered to be  $\mu = 135$  and  $\lambda = 3250$  (kPa). The magnitude of the referential remnant magnetic flux density at each block is  $|\tilde{\mathbb{B}}^r| = 94$  (mT). However, as can be seen from the figure, the direction of  $\tilde{\mathbb{B}}^r$  is not the same in all blocks. To deform the body by magnetic loading, the maximum external magnetic flux density  $|\mathbb{B}_{\max}^{\text{ext}}| = 40$  (mT) is applied along the  $X_3$ -axis.

Due to symmetry in the  $X_1X_2$  plane, only one-quarter of the geometry is discretized. Numerical simulations reveal that a mesh containing 15 elements along  $AC$  and 3 elements along  $AA'$  is sufficient to obtain convergent results. The displacement component  $u_3$  at some material

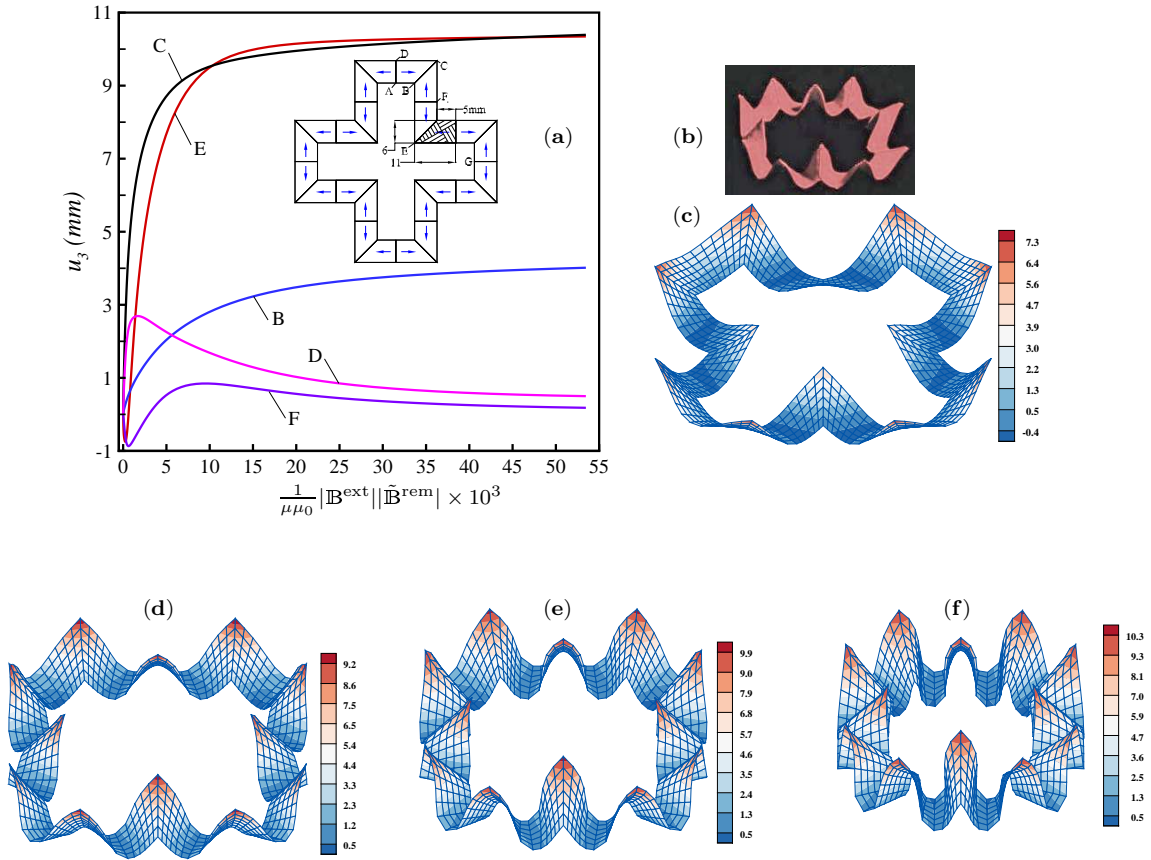


Figure 3: A hollow cross under magnetic loading, (a): load-displacement curves, (b): experiment [18], (c,d,e,f): deformed shapes with the contour plots of  $u_3$  (in mm) for  $|\mathbb{B}^{\text{ext}}| \in \{10, 50, 100, 200\}$  (mT)

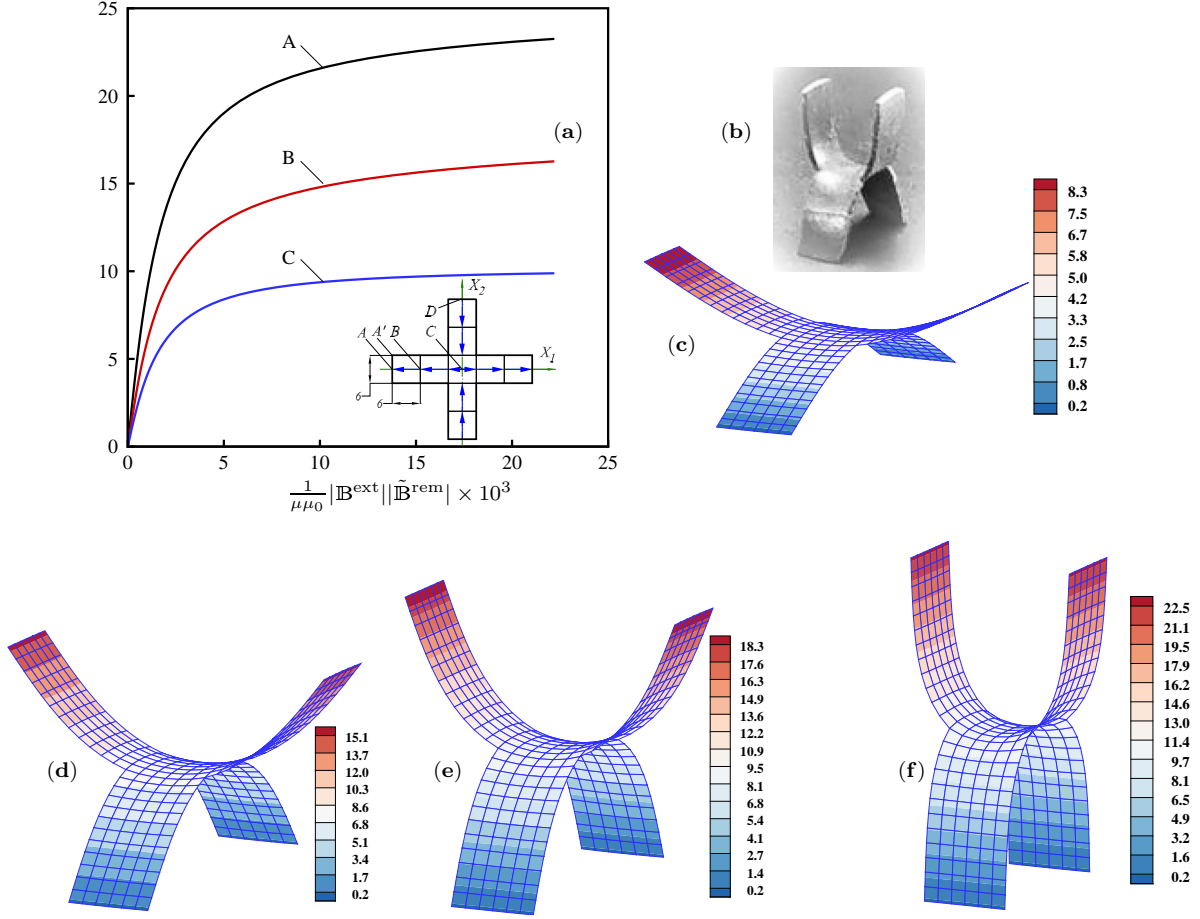


Figure 4: A cross-shaped geometry under magnetic loading, (a): load-displacement curves, (b): experiment [20], (c,d,e,f): deformed shapes with the contour plots of  $u_3$  (in mm) for  $|\mathbb{B}^{\text{ext}}| \in \{2, 5, 10, 40\}$  (mT)

points versus the nondimensional loading parameter  $\frac{10^3}{\mu\mu_0} |\mathbb{B}^{\text{ext}}| |\tilde{\mathbb{B}}^{\text{rem}}|$  is plotted in Fig. 4(a). It is noted that the displacement  $u_3$  of the point  $D$  has been considered to be zero. The maximum lateral displacement occurs at the point  $A$  and is about 22.78 mm. The final deformed shape of the body observed in the experimental studies of Ref. [20] is displayed in Fig. 4(b). Moreover, the deformed shapes of the cross under four different values of the external magnetic flux are illustrated in Figs. 4(c,d,e,f). Obviously, the final deformed shape in Fig. 4(e), predicted by the present formulation, is qualitatively similar to that observed in the experiments of Kuang et al. [20] in Fig. 4(b).

#### 7.4. Deformation of an H-shaped geometry

In this example, the large deformation of an H-shaped geometry under magnetic loading is investigated. As shown in Fig. 5(a), the geometry is composed of 15 blocks, of which dimensions, material, and magnetic properties are the same as those given in the previous example. The maximum external magnetic flux density  $\mathbb{B}_{\max}^{\text{ext}} = -50\mathbf{e}_3$  (mT) is applied to the body.

Due to symmetry, only one-quarter of the geometry is discretized. Numerical simulations indicate that a mesh of  $4 \times 4$  elements in each block is sufficient to obtain convergent results. In other words, the number of elements along  $AA'$ ,  $AC$  and  $CD$  is 2, 14, and 10, respectively. The displacement component  $u_3$  at some material points versus the nondimensional loading parameter  $\frac{10^3}{\mu\mu_0}|\mathbb{B}^{\text{ext}}||\tilde{\mathbb{B}}^{\text{rem}}|$  is displayed in Fig. 5(a). It is noted that the lateral deflection at the point  $D$  is zero. The maximum lateral displacement of about 24.65 mm at the material point  $A$  is observed. The final deformed shape of the body from the experimental observations of Kuang et al. [20] is illustrated in Fig. 5(b). Moreover, the deformed shapes of the body under four different values of the external magnetic flux are displayed in Figs. 5(c,d,e,f). A comparison of figures 5(b) and 5(e) shows that the final deformed shape obtained by the present formulation is qualitatively similar to that observed in the experiments of Kuang et al. [20].

#### 7.5. Deformation of a cylinder (magnetic pump)

In this example, the elastic deformation of a cylindrical shell made of HMSMs and subject to magnetic loading is investigated. As will be shown below, the deformation pattern in the cylinder is so that it may be used as a macro- or micro-fluidic magnetic pump in practical applications. In a relatively similar context, an electro-active polymer-based micro-fluidic pump can be seen in Yan et al. [76]. In the present case, it is assumed that the cylinder has been made of the same blocks as described in the example 7.3. To construct the geometry, 24 blocks in the circumferential direction and 20 blocks along the axis of the cylinder are used. Therefore, the mean radius and length of the cylinder are  $R = 22.9$  and  $L = 120$  (mm), respectively. It is assumed that the remnant magnetic flux  $\tilde{\mathbb{B}}^{\text{rem}}$  is tangent to the cylinder surface, perpendicular to the  $X_2$  axis, and has a positive component along the  $X_3$  axis. The maximum external magnetic flux density  $\mathbb{B}_{\max}^{\text{ext}} = 150\mathbf{e}_3$  (mT) is applied to the body. Moreover, both ends of the cylinder are assumed to be clamped.

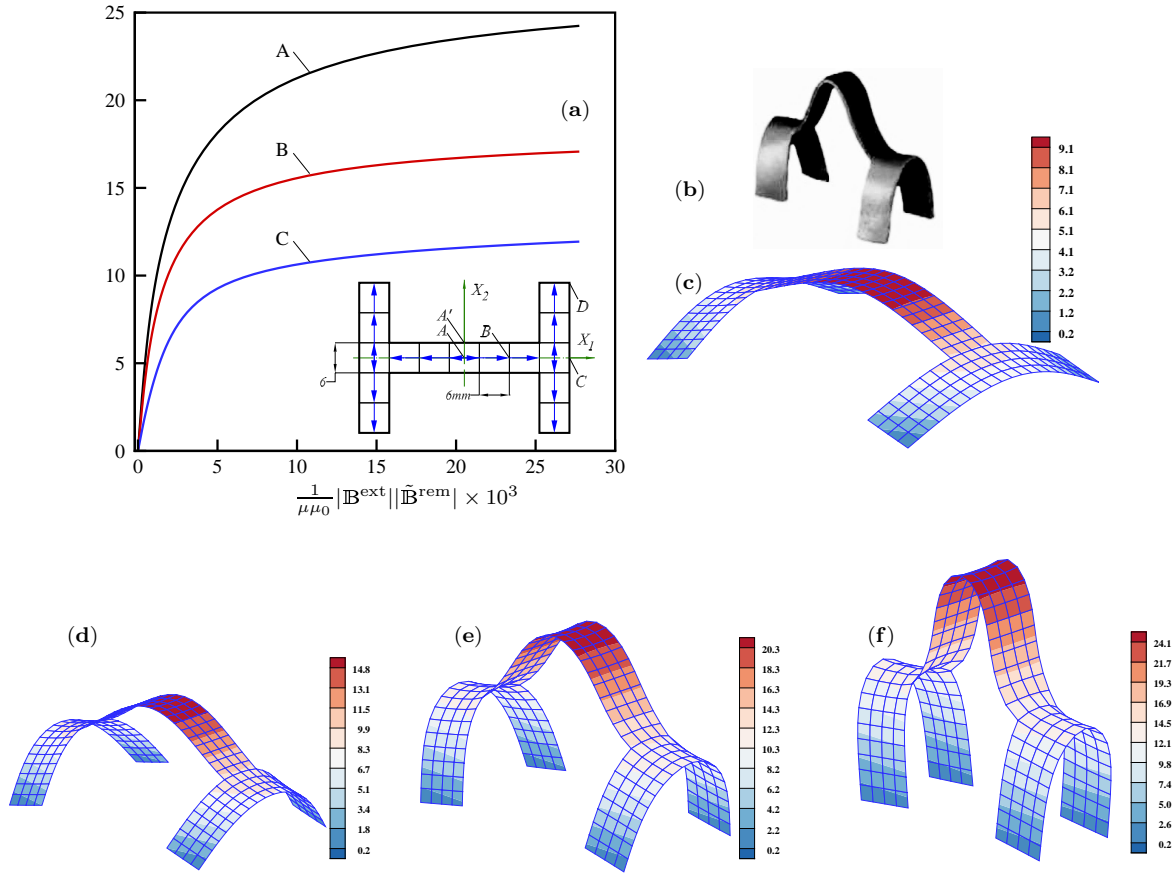


Figure 5: An H-shaped geometry under magnetic loading, (a): load-displacement curves, (b): experiment [20], (c,d,e,f): deformed shapes with the contour plots of  $u_3$  (in mm) for  $|\mathbb{B}^{\text{ext}}| \in \{2, 5, 15, 50\}$  (mT)

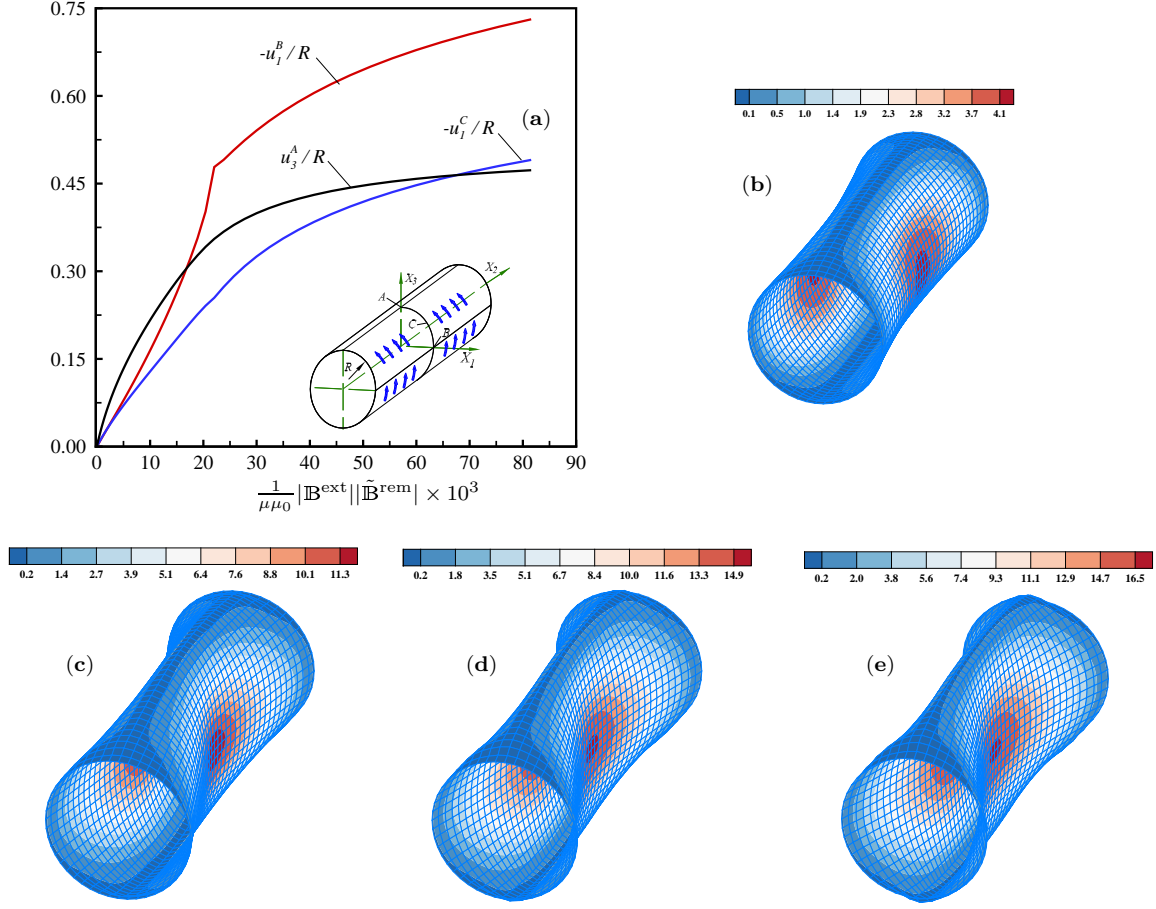


Figure 6: Deformation of a cylinder under magnetic loading, (a): load-displacement curves, (b,c,d,e): deformed shapes with the contour plots of  $|u_1|$  (in mm) for  $|\mathbb{B}^{\text{ext}}| \in \{20, 50, 100, 150\}$  (mT)

Due to symmetry, only one-quarter of the geometry is discretized by the shell elements. Numerical simulations show that a mesh of  $24 \times 20$  elements is sufficient to obtain convergent results. Variations of the displacement components  $u_1$  and  $u_3$  at some material points against the nondimensional loading parameter  $\frac{10^3}{\mu\mu_0} |\mathbb{B}^{\text{ext}}| |\tilde{\mathbb{B}}^{\text{rem}}|$  are plotted in Fig. 6(a). The coordinates of the material points  $A$ ,  $B$  and  $C$ , lying in the  $XZ$ -plane, are  $(0, R)$ ,  $(R, 0)$ , and  $\frac{1}{\sqrt{2}}(R, R)$ , respectively. The maximum (horizontal) displacement occurs at the point  $B$  and is about 16.75 mm. The deformed shapes of the cylinder under four different values of the external magnetic flux are demonstrated in Figs. 5(b,c,d,e). It is observed that under the applied magnetic flux, the cylinder contracts at its middle section. This is the reason why it can be used as a magnetic pump in real applications.

### 7.6. A magnetic gripper

The elastic deformation of a spherical gripper made of HMSMs and subject to magnetic loading is studied in this example. Soft grippers made of magneto-active materials have the potential as actuating components in soft robotics. For instance, Ju et al. [77] and Carpenter et al. [78] demonstrated additively manufactured magneto-active grippers while Kadapa and Hossain [79] simulated the viscoelastic influences of underlying polymeric materials. In our case, the gripper is composed of 12 equal arms. In the undeformed configuration, the arms cover the surface of an incomplete sphere of radius  $R$ . It is assumed that the mechanical and magnetic properties, and the thickness of the HMSM are the same as those given in the example 7.3. The geometry of a single arm is shown in Fig. 7(a). The arc  $DE$  lies in the  $X_1X_2$  plane, its length is 12 mm, and covers  $30^\circ$  of a full circle. Therefore, the mean radius of the arm is  $R = \frac{12}{\pi/6} = 22.92$  mm. The arc  $AC$  lies in the  $X_1X_3$  plane and its length is 60 mm. The angle between the radius  $OA$  and the  $X_3$ -axis is  $15^\circ$ , and the geometry is symmetric w.r.t. the  $X_1X_2$  plane. Moreover, the topmost arc of the arm is assumed to be clamped. As shown in the figure, let  $\mathbf{e}_\varphi$  be the standard meridian unit tangent vector to the sphere. It is assumed that the remnant magnetic flux  $\tilde{\mathbb{B}}^{\text{rem}}$  is along  $\mathbf{e}_\varphi$  for  $X_3 > 0$ , and along  $-\mathbf{e}_\varphi$  for  $X_3 < 0$ . The maximum external magnetic flux density  $\mathbb{B}_{\text{max}}^{\text{ext}} = 10\mathbf{e}_3$  (mT) is applied to the body.

Numerical simulations show that a mesh of  $6 \times 30$  elements in the arm leads to convergent results. Variations of the displacement components  $u_1$  and  $u_3$  at some material points versus the nondimensional loading parameter  $\frac{10^3}{\mu\mu_0}|\mathbb{B}^{\text{ext}}||\tilde{\mathbb{B}}^{\text{rem}}|$  are plotted in Fig. 7(a). For a single arm under the maximum external magnetic flux of 10 mT, the maximum value of the displacement component  $u_3$  is obtained to be about 43.9 mm. The deformed shapes of the gripper under four different values of the external magnetic flux are illustrated in Figs. 7(b,c,d,e). It is noted that the maximum value of the external magnetic flux to avoid intersection between the arms is 6.8 mT. In this case, the maximum  $u_3$  component of displacement is about 41.6 mm.

## 8. Summary

In this research, a 10-parameter micropolar shell model for large elastic deformation analysis of thin structures made of hard-magnetic soft materials was developed. The idea of employing the micropolar theory comes from the fact that an external magnetic flux induces a body couple on



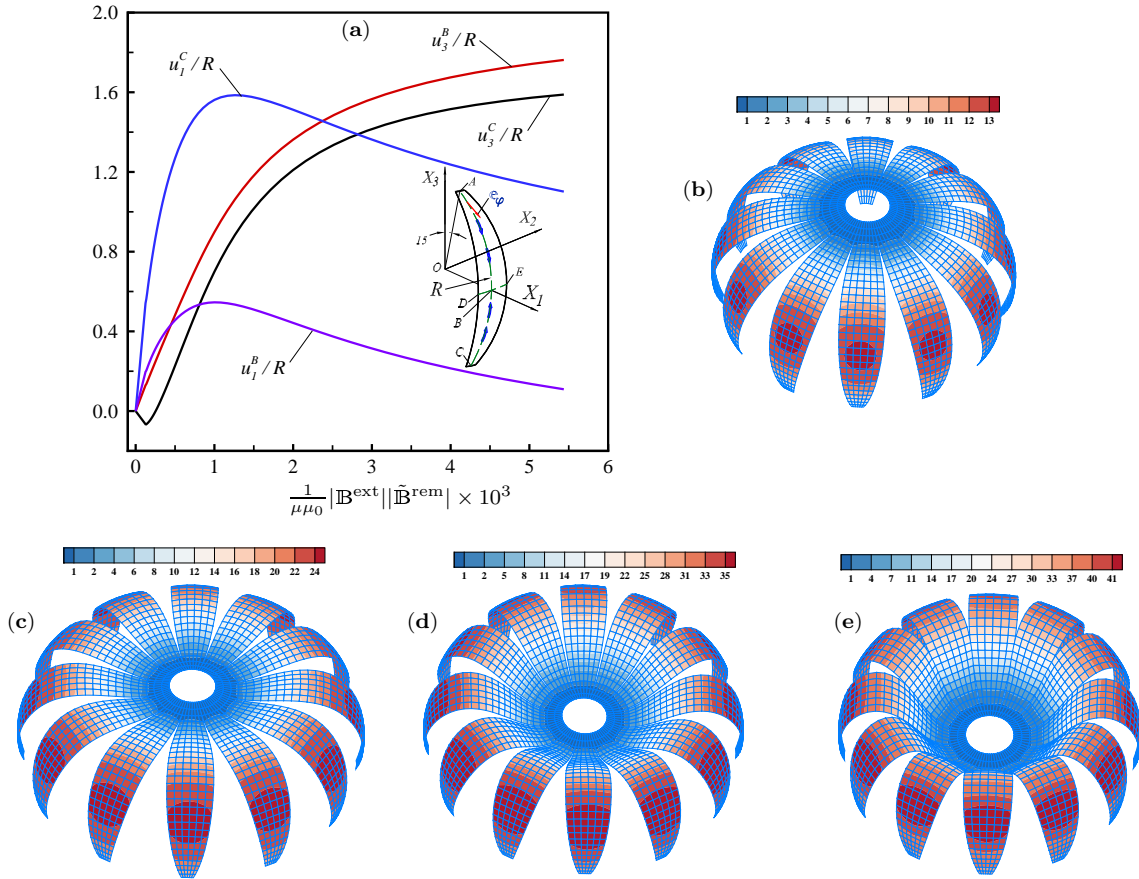


Figure 7: Deformation of a spherical gripper with 12 arms, (a): load-displacement curves, (b,c,d,e): deformed shapes with the contour plots of  $u_3$  (in mm) for  $|\mathbb{B}^{\text{ext}}| \in \{1, 2, 4, 6.8\}$  (mT)

the material particles of HMSMs, which in turn leads to asymmetric Cauchy stress tensor. Since the governing equations at finite strains, including magnetic effects, cannot be solved analytically, a nonlinear finite element formulation for the numerical solution of the governing equations under arbitrary geometry, boundary conditions, and loading cases was developed. Six different numerical examples were solved to investigate the applicability of the developed formulation. It was observed that the present formulation can capture the numerical and experimental results reported in the literature. The generalization of the present research to include thermal and viscoelastic effects will be made in the subsequent contributions.

### **Declaration of competing interest**

The authors declare that they have no known competing financial interests or personal relationships that could have appeared to influence the work reported in this paper.

### **Acknowledgements**

M. Hossain acknowledges the funding through an Engineering and Physical Sciences Research Council (EPSRC) Impact Acceleration Award (EP/R511614/1). M. Hossain also acknowledges the support by EPSRC through the Supergen ORE Hub (EP/S000747/1), which has awarded funding for the Flexible Fund project Submerged bi-axial fatigue analysis for flexible membrane Wave Energy Converters (FF2021-1036).

### **References**

- [1] Z. Ren, W. Hu, X. Dong, M. Sitti, Multi-functional soft-bodied jellyfish-like swimming, *Nature Commun.* 10 (2019) 2703.
- [2] S. Wu, W. Hu, Q. Ze, M. Sitti, R. Zhao, Multifunctional magnetic soft composites: a review, *Multifunct. Mater.* 3 (2020) 042003.
- [3] A.K. Bastola, M. Paudel, L. Li, W. Li, Recent progress of magnetorheological elastomers: a review, *Smart Mater. Struct.* 29 (2020) 123002.

- [4] A.K. Bastola, M. Hossain, The shape-morphing performance of magnetoactive soft materials, *Mat. Des.* 211 (2021) 110172.
- [5] S. Lucarini, M. Hossain, D. Garcia-Gonzalez, Recent advances in hard-magnetic soft composites: synthesis, characterisation, computational modelling, and applications, *Compos. Struct.* 200 (2022) 210001.
- [6] E. Yarali, M. Banishadi, A. Zolfagharian, M. Chavoshi, F. Arefi, M. Hossain, A. Bastola, M. Ansari, A. Foyouzat, A. Dabbagh, M. Ebrahimi, M.J. Mirzaali, M. Bodaghi, Magneto/electroresponsive polymers toward manufacturing, characterization, and biomedical/soft robotic applications, *Appl. Mater. Today.* 26 (2022) 101306.
- [7] P. Saxena, M. Hossain, P. Steinmann, A theory of finite deformation magneto-viscoelasticity, *Int. J. Solids Struct.* 50 (2013) 3886–3897.
- [8] G. Ethiraj, C. Miehe, Multiplicative magneto-elasticity of magnetosensitive polymers incorporating micromechanically-based network kernels, *Int. J. Eng. Sci.* 102 (2016) 93–119.
- [9] M. Mehnert, M. Hossain, P. Steinmann, Towards a thermo-magneto-mechanical coupling framework for magneto-rheological elastomers, *Int. J. Solids Struct.* 128 (2017) 117–132.
- [10] D. Mukherjee, L. Bodelot, K. Danas, Microstructurally-guided explicit continuum models for isotropic magnetorheological elastomers with iron particles, *Int. J. Non-Linear Mech.* 120 (2020) 103380.
- [11] R. Bustamante, M.H.B.M. Shariff, M. Hossain, Mathematical formulations for elastic magneto-electrically coupled soft materials at finite strains: Time-independent processes, *Int. J. Eng. Sci.* 159 (2021) 103429.
- [12] X. Hu, H. Zhu, S. Chen, H. Yu, S. Qu, Magnetomechanical behavior of soft magnetoactive membranes, *Int. J. Solids Struct.* 234–235 (2022) 111310.
- [13] E. Akbari, H. Khajehsaeid, A continuum magneto-mechanical model for magnetorheological elastomers, *Smart Mater. Struct.* 30 (2020) 015008.

- [14] M. Schümann, D.Y. Borin, J. Morich, S. Odenbach, Reversible and non-reversible motion of NdFeB-particles in magnetorheological elastomers, *J. Intell. Mater. Syst. Struct.* 32 (2020) 3–15.
- [15] M. Lee, T. Park, C. Kim, S.M. Park, Characterization of a magneto-active membrane actuator comprising hard magnetic particles with varying crosslinking degrees, *Mater. Des.* 195 (2020) 108921.
- [16] G.Z. Lum, Z. Ye, X. Dong, H. Marvi, O. Erin, W. Hu, M. Sitti, Shape-programmable magnetic soft matter, *Proc. Natl. Acad. Sci.* 113 (2016) 6007–6015.
- [17] S. Wu, Q. Ze, R. Zhang, N. Hu, Y. Cheng, F. Yang, R. Zhao, Symmetry-breaking actuation mechanism for soft robotics and active metamaterials, *ACS Appl. Mater. Interfaces* 11 (2019) 41649–41658.
- [18] Y. Kim, H. Yuk, R. Zhao, S.A. Chester, X. Zhao, Printing ferromagnetic domains for untethered fast-transforming soft materials, *Nature* 558 (2018) 274–279.
- [19] Y. Alapan, A.C. Karacakol, S.N. Guzelhan, I. Isik, M. Sitti, Reprogrammable shapemorphing of magnetic soft machines, *Sci. Adv.* 6 (2020) eabc6414.
- [20] X. Kuang, S. Wu, Q. Ze, L. Yue, Y. Jin, S.M. Montgomery, F. Yang, H.J. Qi, R. Zhao, Magnetic dynamic polymers for modular assembling and reconfigurable morphing architectures, *Adv. Mater.* (2021) 2102113.
- [21] L. Wang, D. Zheng, P. Harker, A.B. Patel, C.F. Guo, X. Zhao, Evolutionary design of magnetic soft continuum robots, *Proc. Natl. Acad. Sci.* 118 (2021) 21.
- [22] S. Wu, C.M. Hamel, Q. Ze, F. Yang, H.J. Qi, R. Zhao, Evolutionary algorithm-guided voxel-encoding printing of functional hard-magnetic soft active materials, *Adv. Intell. Syst.* 2 (2021) 2000060.
- [23] K.A. Kalina, J. Brummund, P. Metsch, M. Kaestner, D.Y. Borin, J.M. Linke, S. Odenbach, Modeling of magnetic hystereses in soft MREs filled with NdFeB particles, *Smart Mater. Struct.* 26 (2017) 105019.

- [24] R. Zhao, Y. Kim, A.S. Chester, P. Sharma, X. Zhao, Mechanics of hard-magnetic soft materials, *J. Mech. Phys. Solids* 124 (2019) 244–263.
- [25] D. Garcia-Gonzalez, Magneto-visco-hyperelasticity for hard-magnetic soft materials: theory and numerical applications, *Smart Mater. Struct.* 28 (2019) 085020.
- [26] D. Mukherjee, M. Rambausek, K. Danas, An explicit dissipative model for isotropic hard magnetorheological elastomers, *J. Mech. Phys. Solids* 151 (2021) 104361.
- [27] M. Rambausek, D. Mukherjee, K. Danas, A computational framework for magnetically hard and soft viscoelastic magnetorheological elastomers, *Comput. Methods Appl. Mech. Engr.* 391 (2022) 114500.
- [28] R. Zhang, S. Wu, Z. Qiji, Z. Zhao, Micromechanics study on actuation efficiency of hard-magnetic soft active materials, *J. Appl. Mech.* 87 (2020) 091008.
- [29] D. Garcia-Gonzalez, M. Hossain, A microstructural-based approach to model magneto-viscoelastic materials at finite strains, *Int. J. Solids Struct.* 208–209 (2021) 119–132.
- [30] D. Garcia-Gonzalez, M. Hossain, Microstructural modelling of hard-magnetic soft materials: Dipole–dipole interactions versus Zeeman effect, *Extreme Mech. Lett.* 48 (2021) 101382.
- [31] H. Ye, Y. Li, T. Zhang, Magttice: A lattice model for hard-magnetic soft materials, *Soft Matter* 17 (2021) 3560–3568.
- [32] F. Dadgar-Rad, M. Hossain, Finite deformation analysis of hard-magnetic soft materials based on micropolar continuum theory, *Int. J. Solids Struct.* 251 (2022) 111747.
- [33] L. Wang, Y. Kim, G.F. Guo, X. Zhao, Hard-magnetic elastica, *J. Mech. Phys. Solids* 142 (2020) 104045.
- [34] W. Chen, Z. Yan, L. Wang, Complex transformations of hard-magnetic soft beams by designing residual magnetic flux density, *Soft Matter* 16 (2020) 6379–6388.
- [35] W. Chen, L. Wang, Z. Yan, B. Luo, Three-dimensional large-deformation model of hard-magnetic soft beams, *Compos. Struct.* 266 (2021) 113822.

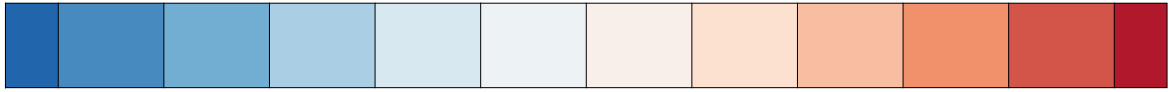
- [36] A. Rajan, A. Arockiarajan, Bending of hard-magnetic soft beams: A finite elasticity approach with anticlastic bending, *Eur. J. Mech. A/Sol.* 90 (2021) 104374.
- [37] D. Yan, A. Abbasi, P.M. Reis, A comprehensive framework for hard-magnetic beams: reduced-order theory, 3D simulations, and experiments, *Int. J. Solids Struct.* (2021) <https://doi.org/10.1016/j.ijsolstr.2021.111319>.
- [38] D. Yan, M. Pezzulla, L. Cruveiller, A. Abbasi, P.M. Reis, Magneto-active elastic shells with tunable buckling strength, *Nature Commun.* 12 (2021) 2831.
- [39] F. Dadgar-Rad, M. Hossain, Large viscoelastic deformation of hard-magnetic soft beams, *Extreme Mech. Lett.* 54 (2022) 101773.
- [40] A. Dorfmann, R.W. Ogden, *Nonlinear Theory of Electroelastic and Magnetoelastic Interactions*, Springer, 2014.
- [41] C.B. Kafadar, A.C. Eringen, Micropolar media—I the classical theory. *Int. J. Eng. Sci.* 9 (1971) 271–307.
- [42] A.C. Eringen, C.B. Kafadar, Polar field theories, in: A.C. Eringen (Ed.), *Continuum Physics*, vol. IV, Academic Press, 1976, pp. 1–73.
- [43] A.C. Eringen, *Microcontinuum Field Theories*, vol. I, Foundations and Solids. Springer, 1999.
- [44] P. Steinmann, K. Willam, Localization within the framework of micropolar elasto-plasticity, in: O. Bruller, V. Mannl, J. Najari, (Eds.), *Advances in Continuum Mechanics*, Springer, 1991, pp. 296–313.
- [45] R. de Borst, A generalization of  $J_2$ -flow theory for polar continua, *Comput. Methods Appl. Mech. Eng.* 103 (1993) 347–362.
- [46] P. Steinmann, A micropolar theory of finite deformation and finite rotation multiplicative elastoplasticity, *Int. J. Solids Struct.* 31 (1994) 1063–1084.
- [47] P. Grammenoudis, C. Tsakmakis, Micropolar plasticity theories and their classical limits. Part I: Resulting model, *Acta Mech.* 189 (2007) 151–175.

- [48] P. Grammenoudis, C. Sator, C. Tsakmakis, Micropolar plasticity theories and their classical limits. Part II: Comparison of responses predicted by the limiting and a standard classical model, *Acta Mech.* 189 (2007) 177–191.
- [49] S. Bauer, W.G. Dettmer, D. Peric, M. Schäfer, Micropolar hyper-elastoplasticity: constitutive model, consistent linearization, and simulation of 3D scale effects, *Int. J. Numer. Meth. Eng.* 91 (2012) 39–66.
- [50] H. Altenbach, V.A. Eremeyev, Strain rate tensors and constitutive equations of inelastic micropolar materials, *Int. J. Plast.* 63 (2014) 3–17.
- [51] S. Ramezani, R. Naghdabadi, S. Sohrabpour, Non-linear finite element implementation of micropolar hypo-elastic materials, *Comput. Methods Appl. Mech. Eng.* 197 (2008) 4149–4159.
- [52] S. Ramezani, R. Naghdabadi, S. Sohrabpour, Constitutive equations for micropolar hyper-elastic materials, *Int. J. Solids Struct.* 46 (2009) 2765–2773.
- [53] W. Pietraszkiewicz, V.A. Eremeyev, On natural strain measures of the non-linear micropolar continuum, *Int. J. Solids Struct.* 46 (2009) 774–787.
- [54] S. Bauer, M. Schäfer, P. Grammenoudis, C. Tsakmakis, Three-dimensional finite elements for large deformation micropolar elasticity, *Comput. Methods Appl. Mech. Eng.* 199 (2010) 2643–2654.
- [55] S. Bauer, W.G. Dettmer, D. Peric, M. Schäfer, Micropolar hyper-elasticity: constitutive model, consistent linearization and simulation of 3D scale effects, *Comput. Mech.* 50 (2012) 383–396.
- [56] S.G. Erdelj, G. Jelenić, A. Ibrahimbegović, Geometrically non-linear 3D finite-element analysis of micropolar continuum, *Int. J. Solids Struct.* 202 (2020) 745–764.
- [57] V.A. Eremeyev, Nonlinear micropolar shells: Theory and applications, in: W. Pietraszkiewicz, C. Szymczak (Eds.), *Shell structures: Theory and applications*, Taylor & Francis, 2005, pp. 11–18.

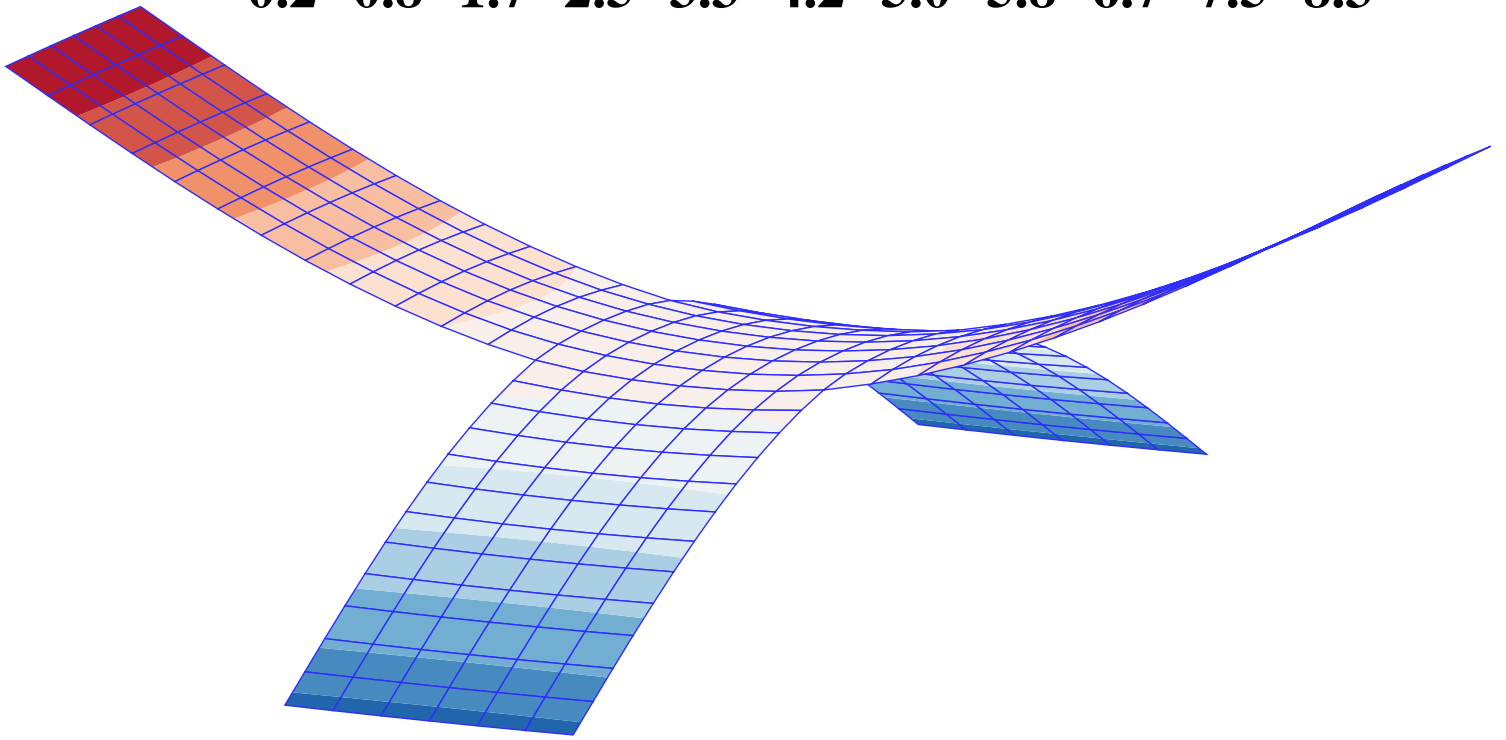
- [58] V.A. Eremeyev, H. Altenbach, Basics of mechanics of micropolar shells, in: H. Altenbach, V.A. Eremeyev (Eds.), *Shell-like Structures*, Springer, 2017, pp 63–111.
- [59] A. Sargsyan, S. Sargsyan, Geometrically nonlinear models of static deformation of micropolar elastic thin plates and shallow shells, *Z. Angew. Math. Mech. (ZAMM)* (2020) e202000148.
- [60] M. Yoder, L. Thompson, J. Summers, Size effects in lattice structures and a comparison to micropolar elasticity, *Int. J. Solids Struct.* 143 (2018) 245–261.
- [61] J.R. Mayeur, D.L. McDowell, D.J. Bammann, Dislocation-based micropolar single crystal plasticity: Comparison of multi- and single criterion theories, *J. Mech. Phys. Solids* 59 (2011) 398–422.
- [62] N. Guarín-Zapata, J. Gomez, C. Valencia, G.F. Dargush, A.R. Hadjesfandiari, Finite element modeling of micropolar-based phononic crystals, *Wave Motion* 92 (2020) 102406.
- [63] A. Spadoni, M. Ruzzene, Elasto-static micropolar behavior of a chiral auxetic lattice, *J. Mech. Phys. Solids* 60 (2012) 156–171.
- [64] I. Goda, M. Assidi, G.F. Ganghoffer, A 3D elastic micropolar model of vertebral trabecular bone from lattice homogenization of the bone microstructure, *Biomech. Model. Mechanobiol.* 13 (2014) 53–83.
- [65] S.S. Suh, W-C. Sun, D.T. O’Connor, A phase field model for cohesive fracture in micropolar continua, *Comput. Methods Appl. Mech. Eng.* 369 (2020) 113181.
- [66] C. Sansour, Large strain deformations of elastic shells, constitutive modelling and finite element analysis, *Comput. Methods Appl. Mech. Engrg.* 161 (1998) 1–18.
- [67] C. Sansour, F.G. Kollmann, Families of 4-node and 9-node finite elements for a finite deformation shell theory, an assessment of hybrid stress, hybrid strain and enhanced strain elements, *Comput. Mech.* 24 (2000) 435–447.
- [68] J.C. Simo, F. Armero, Geometrically non-linear enhanced strain mixed methods and the method of incompatible modes, *Int. J. Numer. Methods Eng.* 33 (1992) 1413–1449.



- [69] J.C. Simo, F. Armero, R.L. Taylor, Improved versions of assumed enhanced strain trilinear elements for 3D finite deformation problems, *Comput. Methods Appl. Mech. Eng.* 110 (1993) 359–386.
- [70] J. Korelc, P. Wriggers, Consistent gradient formulation for a stable enhanced strain method for large deformations, *Eng. Comput.* 13 (1996) 103–123.
- [71] S. Glaser, F. Armero, On the formulation of enhanced strain finite elements in finite deformations, *Eng. Comput.* 14 (1997) 759–791.
- [72] M. Itskov, *Tensor Algebra and Tensor Analysis for Engineers*, Springer, 2019.
- [73] S. Ramezani, R. Naghdabadi, S. Sohrabpour, Analysis of micropolar elastic beams, *Eur. J. Mech. A/Sol* 28 (2009) 202–208.
- [74] P. Wriggers, *Nonlinear Finite Element Methods*, Springer, 2008.
- [75] J. Argyris, An excursion into large rotations, *Comput. Methods Appl. Mech. Eng.* 32 (1982) 85–155.
- [76] B. Yan, B. Li, F. Kunecke, Z. Gu, L. Guo L, Polypyrrole-based implantable electroactive pump for controlled drug microinjection, *ACS Appl. Mater. Interfaces*, 7 (27) (2015) 14563–14568.
- [77] Y. Ju, R. Hu, Y. Xie, J. Yao, X. Li, Y. Lv, X. Han, Q. Cao, L. Li, Reconfigurable magnetic soft robots with multimodal locomotion, *Nano Energy*, 87 (2021) 106169.
- [78] J. A. Carpenter, T. B. Eberle, S. Schuerle, A. Rafsanjani, A. R. Studart, Facile manufacturing route for magneto-responsive soft actuators, *Adv. Intell. Syst.* 3 (2021) 20000283.
- [79] C. Kadapa, M. Hossain, A unified numerical approach for soft to hard magneto-viscoelastically coupled polymers, *Mech. Mat.* 166 (2022) 104207.



**0.2 0.8 1.7 2.5 3.3 4.2 5.0 5.8 6.7 7.5 8.3**





-1.3 -1.0 -0.6 -0.3 0.0 0.3 0.7 1.0 1.3 1.6 2.0 2.3

